IEEE Access
Multidisciplinary : Rapid Review : Open Access Journal

Received 17 March 2026, accepted 4 May 2026, date of publication 11 May 2026, date of current version 14 May 2026.

Digital Object Identifier 10.1109/ACCESS.2026.3691871

RESEARCH ARTICLE

Efficient RF Power Amplification and Combination Over-the-Air Based on Constant-Envelope Components

MARIUS DIACU[1,2], (Graduate Student Member, IEEE), JOÃO GUERREIRO[1,2], (Member, IEEE), RUI DINIS[1,2], (Senior Member, IEEE), JOÃO P. OLIVEIRA[1,3], (Member, IEEE), PAULO MONTEZUMA[1,2], AND PEDRO VIEGAS[1,2]

[1]NOVA School of Science and Technology, NOVA University of Lisbon, 2829-516 Caparica, Portugal
[2]Instituto de Telecomunicações, 1049-001 Lisbon, Portugal
[3]LASI, UNINOVA-CTS, 2829-516 Caparica, Portugal

Corresponding author: Marius Diacu (m.diacu@campus.fct.unl.pt)

This work was supported by the National Funds through Fundação para a Ciência e a Tecnologia (FCT), I.P., and when eligible, co-funded by European Union (EU) Funds through the Instituto de Telecomunicações, with DOI identifier (https://doi.org/10.54499/UID/50008/2025) under Project UID/50008/2025.

ABSTRACT Energy efficiency (EE) and consumption have become critical concerns for mobile telecommunications operators, where the radio access network (RAN) accounts for the majority of the energy consumption. In 4G, 5G, and upcoming 6G systems, the multicarrier waveforms employed, such as orthogonal frequency-division multiplexing (OFDM), pose significant RAN EE challenges due to their high peak-to-average power ratios (PAPRs), imposing strict transmitter-level linearity requirements. However, RF power amplifiers (PAs) display a trade-off between their linearity and efficiency. This work explores power combination over-the-air (PCOA), where four constant-envelope components are individually amplified by switched-mode PAs (SMPAs) and transmitted by a 4×4 microstrip patch antenna array. A 2×2 subarray is allocated to each component, and beamforming is used to combine them at the channel level, minimizing circuit-based power combiner insertion losses. Analytical, optimized sizing strategies are presented for the SMPAs, at the system level, and for the array. Moreover, a high-level PCOA model is developed to simulate the impact of the component-level scalings, PA sizings, noise, insertion losses, array mutual coupling, mutual coupling compensation strategy, steering direction, and path loss on the PCOA system performance. For all scalings, it is shown that PCOA is correctly performed to any steering direction within a sector, introduces array gain, and reduces the interference to neighboring systems, with the array presenting radiation efficiencies as high as 81.4%. This suggests that the PCOA technique can play a key role in addressing the EE-linearity trade-off in upcoming 6G systems.

INDEX TERMS Antenna arrays, beamforming, energy efficiency, mutual coupling, orthogonal frequency-division multiplexing, microstrip patch antenna, peak-to-average power ratio, power amplifier, power combination over-the-air, RF.

I. INTRODUCTION

Energy efficiency (EE) and consumption have become critical concerns for mobile telecommunications operators. This can be attributed to environmental commitments, such as achieving "net zero" emissions [1], along with the fact that energy costs represent a major operational expenditure (OPEX) [2]. In [1], it was shown that the radio access network (RAN) accounts for 76% of the total energy consumption, showing that the it is the dominant target for EE optimization. To this effect, metrics such as the waste factor have been recently proposed for quantifying EE in RANs [3].

The associate editor coordinating the review of this manuscript and approving it for publication was Tae Wook Kim.

In this work, systems which use waveforms based on orthogonal frequency-division multiplexing (OFDM) are considered. This includes 4G, 5G, and upcoming 6G systems. In particular, OFDM with a cyclic prefix (CP) is used in both 4G [4] and 5G [5], meanwhile discrete Fourier transform-spread-OFDM (DFT-s-OFDM) with a CP is only used in 5G [5]. According to [6], both OFDM and DFT-s-OFDM with CPs will continue to be used in 6G. While these waveforms offer high spectral efficiencies (SEs) and resilience to multipath fading [7], they also feature high peak-to-average power ratios (PAPRs) [7], [8]. This last property makes it challenging to achieve high-performance communication while also having an energy-efficient RAN. On one hand, the high-PAPR waveforms impose strict amplification linearity requirements on the RAN's transmitters, to avoid increasing the bit error rates (BERs) [9], [10]. On the other hand, RF power amplifiers (PAs) display a trade-off between their linearity and efficiency, while being the most important factor in the transmitter EE [9]. Consequently, single-branch static-supply architectures which transmit high-PAPR waveforms must use transconductance PAs, which are linear but highly inefficient. Moreover, since the entire waveform must be within the linear amplification region, the PA is operated at an output power back-off (OBO), further lowering its efficiency [9], [11].

Multiple-branch PAs (MBPAs) have been shown to be more successful at efficiently amplifying high-PAPR waveforms [11]. Two main types of MBPA can be identified. Firstly, solutions such as the Doherty PA [12], [13], [14], where the high-PAPR waveform is split among multiple parallel PAs. Secondly, solutions such as the outphasing PA, also known as the linear amplification with nonlinear components (LINC) PA [15], [16], [17], and the quantized digital amplification (QDA) system [18], [19], [20]. These decompose the high-PAPR waveform into constant-envelope components, which are individually amplified by a per-branch PA. Both types need to combine the amplified components, to obtain the output signal. This can be achieved by employing circuit-based power combiners (the conventional approach) or by considering over-the-air (OTA) combination, where beamforming is utilized to perform channel-level component combination [21]. This is shown in [19] and [22], for QDA and outphasing, respectively. There also exist single-branch solutions for more efficienctly amplifying high-PAPR signals, such as the envelope tracking (ET) technique, where the supply voltage follows the envelope of the high-PAPR waveform [23].

Between the aforementioned techniques, QDA is particularly promising. This is because it exhibits a low complexity, does not require the use of digital pre-distortion (DPD), employs highly-efficient switched-mode PAs (SMPAs), and all components are in-phase [18], [19], [20]. Conversely, the Doherty [13], [14] and outphasing [16], [17] PAs often rely on DPD for linearization, which is known to massively increase the complexity and decrease the efficiency [24]. Furthermore, ET PAs [23] and most Doherty PAs [12] employ transconductance PAs, which are less efficient than SMPAs [9], [11]. Even though SMPAs can also be used in outphasing [16], [17], high outphasing angles vastly decrease the efficiency [15]. There exist variants which can reduce this angle [16], [17], [22], [25], however, the out-of-phase sum is intrinsic to outphasing techniques. Moreover, it is shown in [23] that the ET PA supply has a bandwidth "a few times larger" than the modulated signal, which can be a major issue in wideband contexts, and that the envelope shaping can greatly increase the complexity.

In this work, the power combination over-the-air (PCOA) system introduced in [26] is further explored. A four-branch architecture is considered, where a constant-envelope component is assigned to each branch. Each component is then individually amplified a per-branch SMPA. Due to the constant-envelope components, SMPA nonlinearities [9] are not a concern. The amplified components are transmitted by a 4×4 array of microstrip patch antennas, where a 2×2 subarray is allocated to each component. Since OTA combination is performed [21], the use of power combiners is minimized. This, along with the use of SMPAs, means that a very high system-level efficiency is expected, provided that it is also based on an efficient transmitting array. This work constitutes an extension of [26], where the main contributions can be summarized as follows:

- Exploration of three different amplitude distributions at the SMPA outputs, which are referred to as the "component scalings";
- Analytical, optimized sizing strategies for the SMPAs, at the system level, and array, considering different subarray and array-level antenna spacings;
- Microstrip patch antenna and array-level modeling, considering a commercially available substrate, copper as the conductor, and, for the array, mutual coupling;
- Microstrip patch antenna and array-level performance results,including radiation efficiency analysis;
- PCOA performance results, for different steering directions, considering noise, path loss, array mutual coupling, a mutual coupling compensation strategy, and insertion losses.

For all component scalings, it is shown that the PCOA technique correctly and efficiently combines the constant-envelope components, to any steering direction within a sector. It is also shown that the component scalings significantly affect the PCOA performance. Lastly, it is shown that the array presents radiation efficiencies as high as 81.42%.

The remainder of this work is organized into five sections. Section II presents the considered signal decomposition, PCOA architecture, and the main PCOA parameters. Section III presents the theoretical analysis for the input signals, SMPAs, microstrip patch antennas, subarrays, and for the complete array. Section IV presents the sizing strategies and resulting initial configurations for the previously outlined

PCOA components. Section V presents the considered models, adjusted sizings and simulated results for the microstrip patch antennas, array, and PCOA system. Section VI presents the conclusions.

II. ARCHITECTURE AND PCOA SYSTEM CHARACTERIZATION

In this section, an overview of the considered signal decomposition and complete communication system is presented, along with the main parameters considered. As shown in Fig. 1, this communication system is comprised of an $N_b = 4$, $N^{\text{antennas}} = 16$ PCOA transmitter, where N_b is the number of branches and N^{antennas} is the number of antennas, a wireless channel model, and a receiver which is equipped with a single antenna.

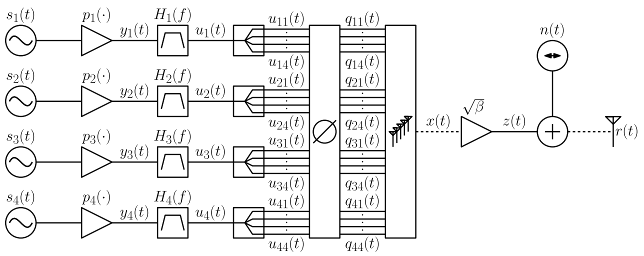

FIGURE 1. High-level diagram of the PCOA transmitter, wireless channel model, and receiver equipped with a single antenna.

The bth PCOA branch, where $b = \{1, 2, 3, 4\}$, has an associated constant-envelope input signal, denoted by $s_b(t)$. In this work, the PCOA transmitter is not paired with a signal decomposition scheme. Thus, it is assumed that the high-PAPR waveform is decomposed into the $s_b(t)$ signals and the signal decomposition is not shown in Fig. 1. While the PCOA technique can be used to transmit the components generated by outphasing [15], [16], [17] and QDA [18], [19], [20], throughout the remainder of this work, a QDA decomposition is assumed. This is due to the advantages outlined in Section I.

In [18], [19], and [20], the QDA decomposition is presented in detail, from which, a brief summary follows. First, the high-PAPR signal (such as OFDM) samples are buffered, to estimate the maximum amplitude of the frame samples. Once the buffer is initially filled, for each new sample, the oldest is removed. All remaining operations solely consider the current sample and estimated maximum frame amplitude value. After undergoing a rectangular to polar form conversion, the sample amplitude is quantized by a normalized quantizer. Based on the quantization bits, each branch is set as ON or OFF. The common phase for all branches is calculated within the polar conversion. Lastly, the components are written by digital-to-analog converters (DACs). They can be written at an intermediate frequency and mixed up, or written by RF DACs at the carrier frequency. When at the carrier frequency, these components constitute the PCOA input signals, $s_b(t)$. Thus, the QDA decomposition presents low complexity, with only a small initial buffering overhead. Considering a buffer that can hold N^{samples} samples, and an OFDM signal with passband B^{passband}, it is shown in [18] that the initial overhead, T^{initial}, is given by $T^{\text{initial}} = N^{\text{samples}}/B^{\text{passband}}$. For $N^{\text{samples}} = 1024$ and $B^{\text{passband}} = 3$ MHz, which is the minimum 5G value [27], it follows that the maximum latency is $T^{\text{initial}} = 0.34$ ms. This is within the most stringent 5G latency specification, namely ≤ 0.5 ms [28]. All DSP operations of the QDA decomposition are performed at baseband, and can be easily implemented through a field programmable gate array (FPGA).

Each branch signal $s_b(t)$ is amplified by an SMPA, represented by the memoryless nonlinear function $p_b(\cdot)$. It follows that $y_b(t) = p_b(s_b(t))$ is the SMPA output signal, which is then filtered by a band-pass filter (BPF), with transfer function $H_b(f)$. With $Y_b(f)$ being the frequency-domain representation of $y_b(t)$, $U_b(f) = Y_b(f)H_b(f)$, where $U_b(f)$ is the frequency-domain representation of the BPF output signal.

Each $u_b(t)$ signal is split by a four-way uniform splitter, resulting in four equal output signals, where the ith is denoted by $u_{bi}(t)$, and $i = \{1, 2, 3, 4\}$. Then, each $u_{bi}(t)$ has a phase shift applied to it, as a part of the beamforming strategy, resulting in the respective $q_{bi}(t)$ signal. It is important to note that all theoretical analysis and simulation results assume ideal splitters and ideal, non-quantized phase shifters. Furthermore, while in Fig. 1 the phase shifters appear as one monolithic block, this is for simplicity. It is also assumed that there exists individual phase control for each $u_{bi}(t)$.

Then, each set of four $q_{bi}(t)$ signals are assigned to a 2×2 subarray. The array thus transmits a total of N^{antennas} $q_{bi}(t)$ signals through its N_b subarrays. The signal $x(t)$ is the combined (far-field) array output signal, which is then affected by the additive white Gaussian noise (AWGN) channel, under line-of-sight (LoS) conditions. Consequently, $z(t) = \sqrt{\beta}x(t)$, where β is the channel gain, and $r(t) = z(t) + n(t)$, where $r(t)$ is the received signal, and $n(t)$ is the channel noise. Thus, a multiple-input, single-output (MISO) context is considered, with no further processing at the receiver (RX) level.

Table 1 summarizes the main PCOA architecture parameters considered. The carrier operating frequency, f_c, is within the 5G frequency range 1 (FR1), and is compliant with the latest 5G RAN specification [27]. The three considered component scalings are equal amplitude scaling (EAS), binary amplitude scaling (BAS), and binary power scaling (BPS). BPS is the main focus of this work, with selected results being presented for all three scalings.

Multipath (fading) channels are not considered in this work. This is justified by the fact that LoS channels can be realistically considered in communication scenarios with uncrewed aerial vehicles (UAVs) or with satellites, where EE is critical. These are scenarios where the proposed highly-efficient PCOA technique can be employed. Moreover, it can be seen in Subsection V-C that the resulting PCOA system is highly directive, substantially reducing the

TABLE 1. Summary of the main PCOA architecture parameters.

Parameter	Value
Operating frequency, f_c	3.5 GHz, band "n78" [27]
Total SMPA output power at f_c, P_y^{total}	30 dBm (1 W)
Characteristic impedance, Z_0	50 Ω
Sector coverage	60° (±30°)
Component scalings	BAS, BPS, EAS
Channel description	AWGN and LoS

effective multipath components. Nevertheless, QDA paired with the proposed PCOA system is an evolution of QDA with combination over-the-air (QDA-CoA) that considers only one transmission antenna per RF component. The QDA-CoA performance considering OFDM signals and Rayleigh fading channels is presented in [19]. There, it is shown that the system is robust to phase errors betwen components of up to 4°, in those conditions. Thus, fading channels do not not disrupt the coherent over-the-air combination of the components. It should be also noted that if accurate channel state information (CSI) is available, the applied phase shifts can be adjusted to counteract the introduced phase mismatches, preserving the in-phase combination [19].

It should also be highlighted that due to the highly directive PCOA transmission (see Subsection V-C), one can expect approximately equal Doppler spreads for each component, since they will have similar angles-of-departure. Therefore, although not considered in this work, Doppler spreads associated to common mobility profiles can be easily corrected by the conventional frequency estimation algorithms.

The high PCOA EE is justified by the fact that all transmissions blocks in Fig. 1 can be efficiently implemented. For the antenna array, since the focus of this work is the theoretical analysis and simulation-based validation of the OTA combination and array properties, an energy-efficient array is designed. The antenna array is shown in Subsection V-B to achieve radiation efficiencies as high as 81.42%. For the phase shifters, due to the $N_b = 4$ branches and $N^{\text{antennas}} = 16$ antennas, hardware-based phase shifters have to be employed. In the literature, several low-loss digital phase shifters are encountered, such as [29], [30], and [31]. These minimize the PCOA complexity, making it very low, and discretize the steering directions. In [29], 2-bit digital phase shifter for the 9.75-11.25 GHz band presented ≤ 0.5 dB of insertion loss. In [30], a 4-bit digital phase shifter presented 1.4 dB of insertion loss at 8 GHz. In [31], a 5-bit digital phase shifter presented 3.26 dB of insertion loss at 2 GHz. For the splitters, their usage is minimized. Only N_b splitters are utilized, to avoid having $N_b = N^{\text{antennas}}$. While transformer-based splitters are known to present several efficiency-related issues [32], efficient Wilkinson splitters can be employed, aided by the fact that the PCOA operation aligns with the ideal Wilkinson conditions. Namely, uniform splitting and zero phase difference between the output ports [33] are followed within all PCOA branches. In [34], a modified Wilkinson combiner/divider was implemented with an insertion loss < 0.2 dB, from 0.3 to 2.8 GHz. In [35], X-band Wilkinson splitters were implemented with 0.2 dB of dissipative loss. In [36], a broadband folded Wilkinson splitter was implemented (reducing the area by 50%) with 2 dB of insertion loss, from 15 to 45 GHz. For the SMPAs, these are known to be highly energy-efficient [9]. In [20], QDA class E SMPAs operating at 880 MHz achieved power-added efficiencies (PAEs) from 63.4% to 69.7%. In [19], QDA class E SMPAs operating between 5.13 GHz and 5.38 GHz were simulated at the circuit level, and achieved PAEs from 64.6% to 73.9%.

III. THEORETICAL ANALYSIS

In this section, the input signals, SMPAs, microstrip patch antennas, subarrays, and the array are theoretically analyzed, in Subsections III-A, III-B, III-C, III-D, and III-E, respectively. These results serve as the basis for the initial sizings, in Section IV.

A. INPUT SIGNALS

Noting that $\omega_c = 2\pi f_c$, each $s_b(t)$ signal is given by

$$s_b(t) = A_b \cos\left(\omega_c t + \vartheta_b\right), \tag{1}$$

where A_b, ϑ_b are the per-branch amplitude and initial phase, respectively. It is important to note that different A_b values can be used to reconstruct the high-PAPR signal envelope, without compromising on the constant-envelope property [11]. This is achieved by considering that each bth branch can be OFF or ON. When it is OFF, $A_b = 0$ V, and when it is ON, A_b has a constant, non-zero value. This is employed in the QDA decomposition [18], [19], [20], and allows the combined amplitude to be varied by selectively toggling the branches ON and OFF. In this work, all branches are assumed to be ON. The relationship between the A_b values and the component scalings is presented in Subsection III-B.

B. SMPAs

Each $p_b(\cdot)$ function is defined as $y_b(t) = p_b\left(s_b\left(t\right)\right) = \alpha_{1b}s_b\left(t\right) + \alpha_{2b}s_b^2\left(t\right) + \alpha_{3b}s_b^3\left(t\right)$, where α_{1b} is the per-branch small-signal gain, and α_{2b}, α_{3b} are the per-branch second and third-order distortion coefficients, respectively [37]. While in implementation SMPAs are strongly nonlinear [9] and can often exhibit memory effects [38], when considering deployment within the PCOA transmitter, the proposed model is not an oversimplification. This is due to two key reasons. Firstly, considering the input signals as defined in Subsection III-A, each SMPA is either OFF, or ON at a constant operating point, dictated by the component scaling. This results in a linear amplification characteristic, where the SMPA nonlinearities have a negligible impact. This model includes the main nonlinear impairments, namely gain compression and harmonics [37], allowing the PCOA robustness with respect to the nonlinear SMPA effects to be demonstrated in Subsection V-C. Secondly, while the PCOA architecture does not compensate for memory effects, the constant, single-tone components allow a quasi-static operation to be assumed for the PCOA system. This is due to the fact that, for signals with bandwidths up to 10 MHz, quasi-static operation at the PA level can be assumed, allowing memory effects to be neglected [39].

Through $s_b(t)$ in (1) and considering the fact that $2\cos(x)\cos(y) = \cos(x-y) + \cos(x+y)$, it follows that

$$y_b(t) = A_{0b} + A_{1b}\cos(\omega_c t + \vartheta_b) + A_{2b}\cos(2\omega_c t + 2\vartheta_b) + A_{3b}\cos(3\omega_c t + 3\vartheta_b), \quad (2)$$

where the coefficients A_{0b} up to A_{3b} are given by

$$A_{0b} = A_{2b} = \frac{\alpha_{2b}A_b^2}{2}, \quad A_{1b} = \alpha_{1b}A_b + \frac{3\alpha_{3b}A_b^3}{4}, \quad A_{3b} = \frac{\alpha_{3b}A_b^3}{4}. \quad (3)$$

As expected, $y_b(t)$ exhibits harmonics and gain compression at the fundamental frequency (see (2)). Ideally, in a linear PA, the voltage gain at the fundamental frequency, G_{vb}, would be α_{1b}. In this work, all SMPA output powers and gains only consider the fundamental frequency term in (2). As such, f_c is omitted from the notation. When considering (1), (2), and (3), it can be concluded that the voltage gain is

$$G_{vb} = \frac{A_{1b}}{A_b} = \frac{\alpha_{1b}A_b + \frac{3\alpha_{3b}A_b^3}{4}}{A_b} = \alpha_{1b} + \frac{3\alpha_{3b}A_b^2}{4}, \quad (4)$$

where it is important to highlight that $\alpha_{1b} > 0$, $\alpha_{2b} \geq 0$, and $\alpha_{3b} \leq 0$ [37]. Consequently, G_{vb} is monotonically decreasing with respect to A_b (see (4)). Thus, the relationship between $s_b(t)$ in (1) and $y_b(t)$ in (2) is only considered for $0 < A_b \leq A_b^{\max}$, where $A_b^{\max}$ is the maximizer of A_{1b}. To find an expression for $A_b^{\max}$, A_{1b} is differentiated with respect to A_b, and the result is set equal to zero, resulting in $A_b^{\max} = \sqrt{-4\alpha_{1b}/(9\alpha_{3b})}$.

Considering (4), it can be seen that the voltage gain at $A_b^{\max}$, denoted by $G_{vb}^{\min}$, is given by $G_{vb}^{\min} = \frac{2}{3}\alpha_{1b}$. Since $G_{vb}^{\min} > 0$, this lets us conclude that $G_{vb} > 0$ for all $0 < A_b \leq A_b^{\max}$. Since the maximum value for A_{1b}, denoted by A_{1b}^{sat}, is given by $A_{1b}^{\text{sat}} = A_b^{\max}G_{vb}^{\min}$, the complete relationship between A_{1b} and A_b can be expressed as

$$A_{1b} = \begin{cases} A_b G_{vb}, & 0 < A_b \leq A_b^{\max} \\ A_{1b}^{\text{sat}}, & A_b > A_b^{\max}. \end{cases} \quad (5)$$

As mentioned in Section I, the component scalings represent different amplitude distributions at the SMPA outputs. More specifically, BAS, BPS, and EAS each represent different ways in which the A_{1b} values are related to a reference amplitude value, denoted by A_1^{ref}. It is thus possible to define them in terms of their vectors of A_{1b} values, $\boldsymbol{A}_1 \in \mathbb{R}^{4\times 1}$, where each A_{1b} value is expressed as a fraction of A_1^{ref}. Denoting the BAS, BPS, and EAS $\boldsymbol{A}_1$ vectors as $\boldsymbol{A}_1^{\text{BAS}}$, $\boldsymbol{A}_1^{\text{BPS}}$, and $\boldsymbol{A}_1^{\text{EAS}}$, respectively, it follows that

$$\begin{aligned} \boldsymbol{A}_1^{\text{BAS}} &= \left[\frac{A_1^{\text{BAS,ref}}}{8} \ \frac{A_1^{\text{BAS,ref}}}{4} \ \frac{A_1^{\text{BAS,ref}}}{2} \ A_1^{\text{BAS,ref}}\right]^T, \\ \boldsymbol{A}_1^{\text{BPS}} &= \left[\frac{A_1^{\text{BPS,ref}}}{2\sqrt{2}} \ \frac{A_1^{\text{BPS,ref}}}{2} \ \frac{A_1^{\text{BPS,ref}}}{\sqrt{2}} \ A_1^{\text{BPS,ref}}\right]^T, \\ \boldsymbol{A}_1^{\text{EAS}} &= \left[A_1^{\text{EAS,ref}} \ A_1^{\text{EAS,ref}} \ A_1^{\text{EAS,ref}} \ A_1^{\text{EAS,ref}}\right]^T, \end{aligned} \quad (6)$$

where $A_1^{\text{BAS,ref}}$, $A_1^{\text{BPS,ref}}$, and $A_1^{\text{EAS,ref}}$ are the BAS, BPS, and EAS A_1^{ref} values, respectively.

Lastly, it is important to note that $y_b(t)$ in (2) is expected to feature intense harmonic distortion, due to the sizing strategy, which is presented in Subsection IV-A. The BPF aims to filter the harmonics and the DC offset, so that, ideally, $u_b(t)$ is only formed by a sinusoidal signal, with frequency f_c. At the circuit level, the SMPA's output matching network is the BPF [9]. Therefore, $H_b(f)$ is known to be high-Q, where Q is the quality factor. This means that it has a narrow bandwidth when compared to f_c [9]. Throughout the remainder of Section III and the entirety of Section IV, it is assumed that all $H_b(f)$ are ideal BPFs with a unitary gain in their passband. Then, in Section V, the $H_b(f)$ considered for modeling and simulation purposes are presented.

C. MICROSTRIP PATCH ANTENNAS

In this work, rectangular microstrip patch antennas are considered. According to [40] and [41], they consist of three layers, namely the top patch, substrate, and ground plane. This is shown in Fig. 2, which presents the considered microstrip patch antenna diagram, orientation and coordinate systems. Moreover, in Fig. 2, φ and θ are the azimuth and elevation angles, respectively, and $\boldsymbol{r}$ is a generic position vector.

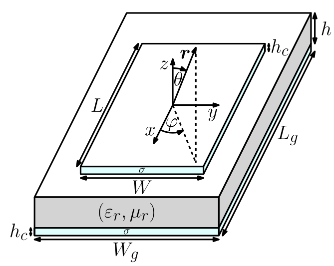

FIGURE 2. Rectangular microstrip patch antenna diagram, along with the consideredorientation and coordinate systems.

The top patch is made of a metal with conductivity σ, and its width, length, and height are denoted by W, L, and h_c, respectively. The substrate is an (ε_r, μ_r) dielectric with height h. The ground plane is made of the same metal as the top patch, with a width and length denoted by W_g and L_g, respectively. The following results assume that $h_c \ll \lambda$, where λ is the free-space wavelength, $h \ll \lambda$, $W_g = L_g = \infty$ m, and that there is a coaxial feed at $(x_f, 0)$ m [40], [41].

According to [40], due to the finite L and W, the fields at the top patch's edges fringe outward. Thus, the electric fields are distributed among the substrate and the surrounding air. For $W \gg h$ and $\varepsilon_r \gg 1$, the fields concentrate mostly in the substrate. Based on this, ε_{reff} is the ε_r of a third, homogeneous dielectric, such that its electrical characteristics match the mixed-dielectric scenario. For $W > h$, and at low frequencies, it follows that

$$\varepsilon_{reff} = \frac{\varepsilon_r + 1}{2} + \frac{\varepsilon_r - 1}{2}\sqrt{\frac{W}{W + 12h}}, \tag{7}$$

and as the frequency increases, ε_{reff} approaches ε_r. Electrically, the top patch appears wider than its physical dimensions, due to the fringing [40]. As such, L_{eff} is the effective L when fringing is taken into account, being given by [41]

$$L_{eff} = L + 2\Delta L, \quad \Delta L \approx c_1 h \frac{\left(\varepsilon_{reff} + \frac{3}{10}\right)\left(\frac{W}{h} + c_2\right)}{\left(\varepsilon_{reff} - c_3\right)\left(\frac{W}{h} + \frac{8}{10}\right)}, \tag{8}$$

where ΔL is the effective length increase for each side, $c_1 = 0.412$, $c_2 = 0.264$, and $c_3 = 0.258$. The resonant frequency, denoted by f_r, is the frequency for which the microstrip patch antenna presents zero reactance in its input impedance, Z_{in}. According to [40], it is given by

$$f_r = \frac{c_0}{2L_{eff}\sqrt{\varepsilon_r}}, \tag{9}$$

where c_0 is the speed of light in a vacuum. In [41], approximate versions of the normalized amplitude beam patterns, denoted by $B_A(\theta, \varphi)$, are presented for the microstrip patch antenna along two planes. Namely, the upper xz half-plane, where $\varphi = 0° \vee \varphi = 180°$, $\theta \in [0°, 90°]$, and the upper yz half-plane, where $\varphi = 90° \vee \varphi = 270°$, $\theta \in [0°, 90°]$. In this work, $B_A(\theta, \varphi)$ is defined as

$$B_A(\theta, \varphi) = \frac{|E(\theta, \varphi)|}{\max\left(|E(\theta, \varphi)|\right)}, \tag{10}$$

where $E(\theta, \varphi)$ is the radiated electric field. Denoting as $B_{\mathrm{Am}}^{xz}(\theta)$ and $B_{\mathrm{Am}}^{yz}(\theta)$ the microstrip patch antenna normalized amplitude beam pattern along the upper xz and yz half-planes, respectively, it follows that

$$\begin{aligned} B_{\mathrm{Am}}^{xz}(\theta) &= \left|\cos\left(\frac{kL\sin(\theta)}{2}\right)\right|, \\ B_{\mathrm{Am}}^{yz}(\theta) &= \left|\frac{2\cos(\theta)}{kW\sin(\theta)}\sin\left(\frac{kW\sin(\theta)}{2}\right)\right|, \end{aligned} \tag{11}$$

where $k = 2\pi/\lambda$ is the wavenumber. It follows that, for the lower xz and yz half-planes, where $\theta \in]90°, 180°]$, $B_{\mathrm{Am}}^{xz}(\theta) = B_{\mathrm{Am}}^{yz}(\theta) = 0$.

D. SUBARRAYS

The results which follow assume subarrays with isotropic antennas. This is motivated by the pattern multiplication theorem, which states that [41], [42]

$$B_A^{\mathrm{array}}(\theta, \varphi) = |\mathrm{AF}(\theta, \varphi)|\, B_A^{\mathrm{antenna}}(\theta, \varphi), \tag{12}$$

where $B_A^{\mathrm{array}}(\theta, \varphi)$ is the normalized amplitude beam pattern for the array and $B_A^{\mathrm{antenna}}(\theta, \varphi)$ is the normalized amplitude beam pattern for an individual array antenna (all antennas are assumed to be equal). Moreover, $|\mathrm{AF}(\theta, \varphi)|$ is the normalized array factor, defined as [42] and [43]

$$|\mathrm{AF}(\theta, \varphi)| = \frac{\left|\boldsymbol{a}^T(\theta, \varphi)\, \boldsymbol{w}(\theta, \varphi)\right|}{\max\left(\left|\boldsymbol{a}^T(\theta, \varphi)\, \boldsymbol{w}(\theta, \varphi)\right|\right)}, \tag{13}$$

where $\boldsymbol{a}^T(\theta, \varphi)$ is the steering vector, encompassing the phase shifts introduced by the channel, and $\boldsymbol{w}(\theta, \varphi)$ is the beamforming weights vector. Thus, if $|\mathrm{AF}(\theta, \varphi)|$ is known, the normalized array beam patterns can then be obtained for any antenna. Since isotropic antennas verify $B_A^{\mathrm{antenna}}(\theta, \varphi) = 1$, by definition, isotropic antenna arrays verify $B_A^{\mathrm{array}}(\theta, \varphi) = |\mathrm{AF}(\theta, \varphi)|$.

Each subarray is an $M_{\mathrm{s}} \times N_{\mathrm{s}}$ uniform planar array (UPA), lying on the xy plane, with horizontal and vertical antenna spacings denoted by δ_{xs} and δ_{ys}, respectively. In Fig. 3, an $M \times N$ UPA of generic elements, lying on the xy plane, with horizontal and vertical element spacings denoted by δ_x and δ_y, respectively, is shown. This lets us conclude that the subarrays correspond to Fig. 3, when considering that the elements are isotropic antennas, $M = M_{\mathrm{s}}$, $N = N_{\mathrm{s}}$, $\delta_x = \delta_{xs}$, and $\delta_y = \delta_{ys}$.

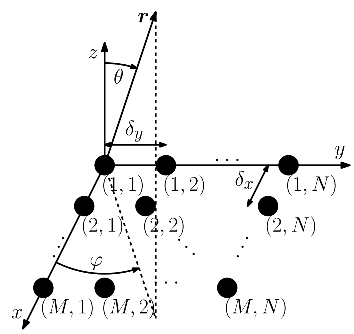

FIGURE 3. UPA with generic elements, along with distinct horizontal and vertical element spacings. The considered UPA orientation and coordinate systems arealso presented.

It should also be noted that, in Fig. 3, $\boldsymbol{r}$ is a generic position vector, and the notation (m, n) denotes element indexing, not xy coordinates. Thus, the subarray antenna (1,1), considered as the reference antenna, is situated at the origin.

To determine the array factor, it is first necessary to define the subarray-level beamforming weights vector [42], denoted by $\boldsymbol{w}_{\mathrm{s}} \in \mathbb{C}^{M_{\mathrm{s}}N_{\mathrm{s}} \times 1}$. Equal amplitude weights are considered, due to the uniform splitting of the $u_b(t)$ signals. For the phases, progressive phase shifts [41] are considered along both x and y directions, denoted by ϕ_{xs} and ϕ_{ys}, respectively. Thus, $\boldsymbol{w}_{\mathrm{s}}$ as a function of the phase shifts, $\boldsymbol{w}_{\mathrm{s}}\left(\phi_{xs}, \phi_{ys}\right)$, is given by

$$\boldsymbol{w}_{\mathrm{s}}\left(\phi_{xs},\phi_{ys}\right)=\begin{bmatrix} e^{j\left((1-1)\phi_{xs}+(1-1)\phi_{ys}\right)} \\ \cdots \\ e^{j\left((M_{\mathrm{s}}-1)\phi_{xs}+(1-1)\phi_{ys}\right)} \\ \cdots \\ e^{j\left((1-1)\phi_{xs}+(N_{\mathrm{s}}-1)\phi_{ys}\right)} \\ \cdots \\ e^{j\left((M_{\mathrm{s}}-1)\phi_{xs}+(N_{\mathrm{s}}-1)\phi_{ys}\right)} \end{bmatrix}, \tag{14}$$

where it can be seen that it corresponds to maximum-ratio transmission (MRT) [43] without the normalization factor. Considering $\boldsymbol{w}_{\mathrm{s}}\left(\phi_{xs},\phi_{ys}\right)$ in (14), the LoS channel model of Table 1, and $\psi_{xs} = k\delta_{xs}\sin(\theta)\cos(\varphi)+\phi_{xs}$, $\psi_{ys} = k\delta_{ys}\sin(\theta)\sin(\varphi)+\phi_{ys}$, it is possible to conclude that the normalized subarray-level array factor, $\left|\mathrm{AF}_{\mathrm{s}}\left(\psi_{xs},\psi_{ys}\right)\right|$, is given by [42]

$$\left|\mathrm{AF}_{\mathrm{s}}\left(\psi_{xs},\psi_{ys}\right)\right|=\frac{1}{M_{\mathrm{s}}N_{\mathrm{s}}}\left|\frac{\sin\left(\frac{M_{\mathrm{s}}\psi_{xs}}{2}\right)\sin\left(\frac{N_{\mathrm{s}}\psi_{ys}}{2}\right)}{\sin\left(\frac{\psi_{xs}}{2}\right)\sin\left(\frac{\psi_{ys}}{2}\right)}\right|, \tag{15}$$

where it can be noted that its maximum is achieved when $\left(\psi_{xs},\psi_{ys}\right) = (0°, 0°)$. Since ψ_{xs} depends on ϕ_{xs} and ψ_{ys} depends on ϕ_{ys}, it is possible to steer the maximum to the direction $(\varphi_{\mathrm{s}}^{\max},\theta_{\mathrm{s}}^{\max})$, by setting ϕ_{xs} and ϕ_{ys} to

$$\begin{aligned}\phi_{xs}&=-k\delta_{xs}\sin\left(\theta_{\mathrm{s}}^{\max}\right)\cos\left(\varphi_{\mathrm{s}}^{\max}\right),\\ \phi_{ys}&=-k\delta_{ys}\sin\left(\theta_{\mathrm{s}}^{\max}\right)\sin\left(\varphi_{\mathrm{s}}^{\max}\right).\end{aligned} \tag{16}$$

E. ARRAY

The results which follow assume that all subarrays are equal. As a consequence, we can recursively apply (12). Namely, each subarray is now seen as an array-level element [42]. This means that determining the array-level normalized array factor, $|\mathrm{AF}_{\mathrm{r}}(\theta,\varphi)|$, lets us find the normalized beam patterns for any subarray. Since $N_b = 4$, the array is a 2×2 UPA of subarrays. The array is considered to be lying on the xy plane, with horizontal and vertical element spacings denoted by δ_{xr} and δ_{yr}, respectively. Thus, it corresponds to Fig. 3 when considering that the elements are subarrays, $M = 2$, $N = 2$, $\delta_x = \delta_{xr}$, and $\delta_y = \delta_{yr}$. Furthermore, the element indexing in Fig. 3 is also considered, where the element (1,1) is taken as the reference.

In conventional MISO array analysis, it is assumed that each element is excited by the same input signal, before applying beamforming [43]. However, this is not the case of the proposed PCOA transmitter. The array-level input signals are the $u_b(t)$ signals ($N_b = 4$). Considering $y_b(t)$ as defined in (2), each signal $u_b(t)$ can be expressed as

$$\begin{aligned}u_b(t)&=A_{1b}\cos\left(\omega_c t+\vartheta_{ub}\right) \Leftrightarrow\\ u_b(t)&=A_{\mathrm{r}b}A_c\cos\left(\omega_c t+\vartheta_{ub}\right),\end{aligned} \tag{17}$$

where ϑ_{ub} is the phase after $H_b(f)$, and A_{1b} is decomposed into a constant value between all branches, A_c, and a per-branch scaling factor, $A_{\mathrm{r}b}$, such that $A_{1b} = A_{\mathrm{r}b}A_c$. Assuming $\vartheta_{u1} = \vartheta_{u2} = \vartheta_{u3} = \vartheta_{u4} = \vartheta_u$, it follows that $u_b(t) = A_{\mathrm{r}b}u(t)$, where $u(t) = A_c\cos\left(\omega_c t+\vartheta_u\right)$ is a common signal to all branches. Thus, at the array level, this scenario can be seen as the transmission of $u(t)$ with the per-branch amplitude weights $A_{\mathrm{r}b}$ applied in $\boldsymbol{w}_{\mathrm{r}} \in \mathbb{C}^{4\times 1}$, the array-level beamforming weights vector [42]. Furthermore, the array-level amplitude weights vector, $\boldsymbol{A}_{\mathrm{r}} \in \mathbb{R}^{4\times 1}$, containing the $A_{\mathrm{r}b}$ weights, verifies $\boldsymbol{A}_{\mathrm{r}} = \boldsymbol{A}_1/A_c$. This means that the component scalings affect the array beamforming, since the $\boldsymbol{A}_{\mathrm{r}}$ and $\boldsymbol{A}_1$ vectors are directly proportional. For the phases, progressive phase shifts [41] along the x and y directions, denoted as ϕ_{xr} and ϕ_{yr}, respectively, are considered. By defining the vector encompassing the applied phase shifts as $\phi_{\mathrm{r}} \in \mathbb{R}^{4\times 1}$, it follows that $\boldsymbol{A}_{\mathrm{r}}$ and ϕ_{r} are given by

$$\boldsymbol{A}_{\mathrm{r}}=\begin{bmatrix}A_{\mathrm{r}(1,1)}\\A_{\mathrm{r}(2,1)}\\A_{\mathrm{r}(1,2)}\\A_{\mathrm{r}(2,2)}\end{bmatrix},\quad \phi_{\mathrm{r}}=\begin{bmatrix}e^{j\left((1-1)\phi_{xr}+(1-1)\phi_{yr}\right)}\\e^{j\left((2-1)\phi_{xr}+(1-1)\phi_{yr}\right)}\\e^{j\left((1-1)\phi_{xr}+(2-1)\phi_{yr}\right)}\\e^{j\left((2-1)\phi_{xr}+(2-1)\phi_{yr}\right)}\end{bmatrix}, \tag{18}$$

respectively, where the notation $A_{\mathrm{r}b} = A_{\mathrm{r}(m,n)}$ denotes that the bth branch is assigned to the element with indices (m, n). Consequently, $\boldsymbol{w}_{\mathrm{r}}$ as a function of $\boldsymbol{A}_{\mathrm{r}}$ and ϕ_{r} is given by

$$\boldsymbol{w}_{\mathrm{r}}(\boldsymbol{A}_{\mathrm{r}},\phi_{\mathrm{r}})=\begin{bmatrix}A_{\mathrm{r}(1,1)}e^{j\left((1-1)\phi_{xr}+(1-1)\phi_{yr}\right)}\\A_{\mathrm{r}(2,1)}e^{j\left((2-1)\phi_{xr}+(1-1)\phi_{yr}\right)}\\A_{\mathrm{r}(1,2)}e^{j\left((1-1)\phi_{xr}+(2-1)\phi_{yr}\right)}\\A_{\mathrm{r}(2,2)}e^{j\left((2-1)\phi_{xr}+(2-1)\phi_{yr}\right)}\end{bmatrix}. \tag{19}$$

Considering $\boldsymbol{w}_{\mathrm{r}}(\boldsymbol{A}_{\mathrm{r}},\phi_{\mathrm{r}})$ in (19), the LoS chanel model of Table 1, and $\psi_{xr} = k\delta_{xr}\sin(\theta)\cos(\varphi)+\phi_{xr}$, $\psi_{yr} = k\delta_{yr}\sin(\theta)\sin(\varphi)+\phi_{yr}$, it is possible to determine $\left|\mathrm{AF}_{\mathrm{r}}\left(\psi_{xr},\psi_{yr}\right)\right|$. However, a closed-form solution is not available for an arbitrary $\boldsymbol{A}_{\mathrm{r}}$, leading to $\left|\mathrm{AF}_{\mathrm{r}}\left(\psi_{xr},\psi_{yr}\right)\right|$ being expressed as [41]

$$|\mathrm{AF}_{\mathrm{r}}|=\frac{\left|\sum_{n=1}^{2}\sum_{m=1}^{2}A_{\mathrm{r}(m,n)}e^{j\left((m-1)\psi_{xr}+(n-1)\psi_{yr}\right)}\right|}{\sum_{n=1}^{2}\sum_{m=1}^{2}A_{\mathrm{r}(m,n)}}, \tag{20}$$

where it can be noted that its maximum value is also achieved when $\left(\psi_{xr},\psi_{yr}\right) = (0°, 0°)$, since this is when the $A_{\mathrm{r}(m,n)}$ terms sum in-phase. Thus, steering the maximum to the direction $(\varphi_{\mathrm{r}}^{\max},\theta_{\mathrm{r}}^{\max})$ does not depend on $\boldsymbol{A}_{\mathrm{r}}$, and can be done by setting ϕ_{xr} and ϕ_{yr} to

$$\begin{aligned}\phi_{xr}&=-k\delta_{xr}\sin\left(\theta_{\mathrm{r}}^{\max}\right)\cos\left(\varphi_{\mathrm{r}}^{\max}\right),\\ \phi_{yr}&=-k\delta_{yr}\sin\left(\theta_{\mathrm{r}}^{\max}\right)\sin\left(\varphi_{\mathrm{r}}^{\max}\right).\end{aligned} \tag{21}$$

Considering (12), $\left|\mathrm{AF}_{\mathrm{s}}\left(\psi_{xs},\psi_{ys}\right)\right|$ as defined in (15), and $\left|\mathrm{AF}_{\mathrm{r}}\left(\psi_{xr},\psi_{yr}\right)\right|$ as defined in (20), it can be concluded that

$$\left|\mathrm{AF}_{\mathrm{t}}(\psi_{xr},\psi_{yr},\psi_{xs},\psi_{ys})\right|=|\mathrm{AF}_{\mathrm{r}}|\,|\mathrm{AF}_{\mathrm{s}}|, \tag{22}$$

where $\left|\mathrm{AF}_{\mathrm{t}}(\psi_{xr},\psi_{yr},\psi_{xs},\psi_{ys})\right|$ is the normalized complete array factor. This allows the normalized complete amplitude beam pattern, $B_{\mathrm{At}}(\psi_{xr},\psi_{yr},\psi_{xs},\psi_{ys})$, to be determined for any antenna by considering (12) once again, with $\left|\mathrm{AF}_{\mathrm{t}}(\psi_{xr},\psi_{yr},\psi_{xs},\psi_{ys})\right|$ as the array factor.

IV. INITIAL SIZINGS AND OPTIMIZATIONS

In this section, the initial sizings for the SMPAs, microstrip patch antennas, subarrays, and array are determined, in Subsections IV-A, IV-B, IV-C, and IV-D, respectively. These values are then used for the initial simulations, in Section V.

A. SMPAs

As seen in Subsection III-B, the component scalings are defined in terms of the A_{1b} values. Since, for operation below $A_b^{\max}$, $A_{1b} = A_b G_{vb}$ (see (5)), it follows that each branch has two degrees of freedom in order to obtain the necessary A_{1b} value. The following analysis is expressed in terms of signal power, P. For a sinusoidal signal, the relationship between its P and amplitude, A, is given by $(2Z)P = A^2$, where Z is the impedance, which is assumed to be purely resistive [44]. Moreover, it is important to note that a generic power gain, G_p, and voltage gain, G_v, are related through [37]

$$G_p = \frac{Z_{in}}{Z_{out}} G_v^2$$
$$\Leftrightarrow 10\log_{10}\left(G_p\right) = 20\log_{10}\left(G_v\right) + 10\log_{10}\left(\frac{Z_{in}}{Z_{out}}\right), \tag{23}$$

where Z_{out} is the output impedance. The considered sizing strategy assumes operation below $A_b^{\max}$, that all $Z_{in} = Z_{out} = Z_0$, and starts with determining the power of each SMPA output signal $y_b(t)$, at f_c, denoted by P_{yb}. This is done considering P_y^{total}, the total SMPA output power at f_c, presented in Table 1, and the component scalings (see (6)). Due to the ideal BPFs, the $u_b(t)$ signal powers, denoted by P_{ub}, verify $P_{ub} = P_{yb}$. Then, the α_{1b}, α_{2b}, and α_{3b} coefficients of each nonlinear SMPA function are determined. This is done by considering that the P_{yb} values are close to the per-branch saturation powers [19], denoted by P_{1b}^{sat}, and that $G_{p1} = G_{p2} = G_{p3} = G_{p4}$, where G_{pb} is the power version of G_{vb} (see (23)). Lastly, the necessary per-branch input signal powers, P_{sb}, are then determined, based on P_{yb} and G_{pb}.

Since the A_{1b} values define the component scalings, at the amplitude level (see (6)), it follows that the P_{yb} values define the component scalings, at the power level. Analogously, they can be defined in terms of their vectors of P_{yb} values, $\boldsymbol{P}_y \in \mathbb{R}^{4\times 1}$, where each P_{yb} is expressed as a fraction of the reference power, P_y^{ref}. Denoting the BAS, BPS, and EAS $\boldsymbol{P}_y$ vectors as $\boldsymbol{P}_y^{\text{BAS}}$, $\boldsymbol{P}_y^{\text{BPS}}$, and $\boldsymbol{P}_y^{\text{EAS}}$, respectively, it follows that

$$\boldsymbol{P}_y^{\text{BAS}} = \left[\frac{P_y^{\text{BAS,ref}}}{64}\ \frac{P_y^{\text{BAS,ref}}}{16}\ \frac{P_y^{\text{BAS,ref}}}{4}\ P_y^{\text{BAS,ref}}\right]^T,$$
$$\boldsymbol{P}_y^{\text{BPS}} = \left[\frac{P_y^{\text{BPS,ref}}}{8}\ \frac{P_y^{\text{BPS,ref}}}{4}\ \frac{P_y^{\text{BPS,ref}}}{2}\ P_y^{\text{BPS,ref}}\right]^T,$$
$$\boldsymbol{P}_y^{\text{EAS}} = \left[P_y^{\text{EAS,ref}}\ P_y^{\text{EAS,ref}}\ P_y^{\text{EAS,ref}}\ P_y^{\text{EAS,ref}}\right]^T, \tag{24}$$

where $P_y^{\text{BAS,ref}}$, $P_y^{\text{BPS,ref}}$, and $P_y^{\text{EAS,ref}}$ are the reference power values for BAS, BPS, and EAS, respectively. Noting that $\boldsymbol{P}_y = [P_{y1}\ \ P_{y2}\ \ P_{y3}\ \ P_{y4}]^T$ and $P_{y1} + P_{y2} + P_{y3} + P_{y4} = P_y^{\text{total}}$, it follows that $P_y^{\text{BAS,ref}} = (64/85)P_y^{\text{total}}$, $P_y^{\text{BPS,ref}} = (8/15)P_y^{\text{total}}$, and $P_y^{\text{EAS,ref}} = P_y^{\text{total}}/4$.

Importantly, G_{vb} does not depend on α_{2b} (see (4)). This conclusion also holds for G_{pb} (see (23)), which allows us to conclude that, in this context, α_{2b} is less important, with the focus being the determination of α_{3b} for a given α_{1b} and P_{yb}. Since the input amplitude of each branch, A_b, is constant (see (1)), the resulting A_{1b} also is, through (5). Consequently, the value of P_{yb} is also constant, allowing each branch SMPA to be optimized for maximum efficiency, as was done in [19]. There, considering per-branch class E SMPAs, it is shown that each SMPA achieves its maximum PAE when operating close to the respective P_{1b}^{sat}.

It is important to note that, at P_{1b}^{sat}, the associated power gain is $G_{pb}^{\min}$, the power version of $G_{vb}^{\min}$. Considering that $G_{vb}^{\min} = \frac{2}{3}\alpha_{1b}$ and (23), it can be concluded that $G_{pb}^{\min}$ presents a gain compression of $c_f^{\max} \approx 3.52$ dB, when compared to the ideal per-branch power gain, $G_{pb}^{\text{ideal}} = 20\log_{10}(\alpha_{1b})$, always assumed to be expressed in dB. Comparatively, at the 1-dB compression point, $c_f = 1$ dB. Accordingly, the sizing strategy is to obtain all P_{yb} at $c_f < c_f^{\max}$ dB of gain compression, where c_f is the compression factor, and $c_f^{\max}$ is the maximum c_f. Operation at close to P_{1b}^{sat} thus corresponds to setting c_f close to $c_f^{\max}$. By definition, c_f dB of gain compression means that $G_{pb} = G_{pb}^{\text{ideal}} - c_f$, with G_{pb} expressed in dB. Considering both, it can be written that

$$20\log_{10}(G_{vb}) = 20\log_{10}(\alpha_{1b}) - c_f$$
$$\Leftrightarrow \alpha_{3b} = \frac{4\left(10^{\frac{G_{pb}^{\text{ideal}}-c_f}{20}} - 10^{\frac{G_{pb}^{\text{ideal}}}{20}}\right)}{6P_{yb}Z_{out}\,10^{\frac{-G_{pb}^{\text{ideal}}+c_f}{10}}}, \tag{25}$$

with G_{vb} defined in (4), and where it is noted that $A_{1b}^2 = A_b^2 G_{vb}^2$, along with $G_{pb}^{\text{ideal}} - c_f = 20\log_{10}(G_{vb})$, allowing α_{3b} to be expressed only in terms of G_{pb}^{ideal}, c_f, P_{yb}, and Z_{out}.

The input signal power values, P_{sb}, are determined by noting that $P_{sb} = P_{yb}/G_{pb}$, with G_{pb} in linear units. It can be noted that the SMPA model coefficients, α_{1b}, α_{2b}, and α_{3b}, can also be expressed through G_{pb}^{ideal}, along with the per-branch second-order input intercept point (IIP2) and the third-order input intercept point (IIP3). For the PCOA input signals defined in (1), intermodulation distortion (IMD) is not a concern. The IIP2 and IIP3 arise when considering a two-tone input signal, $s_{bt}(t) = A_b\cos(\omega_1 t) + A_b\cos(\omega_2 t)$. The resulting per-branch input amplitudes for the IIP2 and IIP3, denoted by A_{IIP2b} and A_{IIP3b}, respectively, are given by [9]

$$A_{IIP2b} \approx \left|\frac{\alpha_{1b}}{\alpha_{2b}}\right|, \quad A_{IIP3b} \approx \sqrt{\frac{4}{3}\left|\frac{\alpha_{1b}}{\alpha_{3b}}\right|}. \tag{26}$$

For $P_y^{\text{total}} = 1$ W, $Z_{in} = Z_{out} = Z_0 = 50\ \Omega$, along with $G_{pb}^{\text{ideal}} = 16$ dB, $P_{IIP2} = 50$ dBm, and $c_f = 2$ dB, Table 2 shows the initial sizing for the SMPA coefficients, P_{yb}, and P_{sb}, for BAS, BPS, and EAS. Furthermore, Fig. 4 shows the relationship between P_{yb} and P_{sb} for the resulting $p_b(\cdot)$ functions, only for BPS.

TABLE 2. Initial sizings for the per-branch SMPA coefficients, fundamental-frequency output power, and input power, considering BAS, BPS, and EAS.

Scaling	b	P_{sb} (dBm)	P_{yb} (dBm)	G_{pb}^{ideal} (dB)	P_{IIP2b} (dBm)	P_{IIP3b} (dBm)
BAS	1	-3.29	10.71	16	50	3.57
	2	2.73	16.73	16	50	9.59
	3	8.75	22.75	16	50	15.62
	4	14.77	28.77	16	50	21.64
BPS	1	4.24	18.24	16	50	11.11
	2	7.25	21.25	16	50	14.12
	3	10.26	24.26	16	50	17.13
	4	13.27	27.27	16	50	20.14
EAS	1	9.98	23.98	16	50	16.85
	2	9.98	23.98	16	50	16.85
	3	9.98	23.98	16	50	16.85
	4	9.98	23.98	16	50	16.85

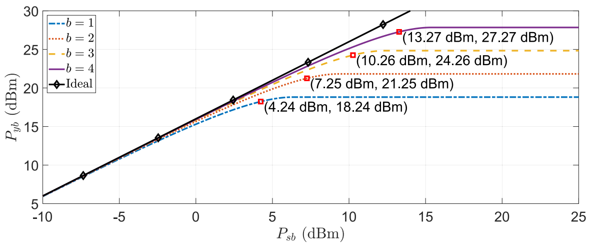

FIGURE 4. SMPA fundamental frequency output power as a function of the input power, for each branch, BPS, and the coefficients inTable 2.

The P_{IIP2b} and P_{IIP3b} are the power version of A_{IIP2b} and A_{IIP3b}, respectively. The G_{pb}^{ideal} and P_{IIP2b} values are not a part of the sizing strategy, and feasible values are instead chosen.

It can be seen in Fig. 4 that the operating points, indicated by the squares, feature P_{yb} values approximately 0.57 to 0.58 dB below P_{1b}^{sat}. Thus, the considered c_f value satisfies the sizing goals. Also pertaining to the operating points, in Fig. 4, it can be seen that all of them verify $G_{pb} = 14$ dB, as intended. This is concluded by noting that $G_{pb} = P_{yb} - P_{sb}$, when G_{pb} is expressed in dB and P_{yb}, P_{sb} in dBm. Considering the $b = 4$ branch as an example, $G_{p4} = P_{y4} - P_{s4} = (27.27 - 13.27)$ dBm $= 14$ dB.

B. MICROSTRIP PATCH ANTENNAS

The rectangular microstrip patch antenna sizing strategy aims to determine W, L, and x_f, such that $f_r = f_c$ and $Z_{in} = Z_0$, assuming that ε_r and h are known. The h_c, σ, W_g, and L_g values are not considered as a part of the initial sizing strategy, and are specified in Subsection V-A.

The following results assume the conditions presented in Subsection III-C. For W, a value which leads to high radiation efficiencies is given by [40]

$$W = \frac{c_0}{2f_c}\sqrt{\frac{2}{\varepsilon_r + 1}} = \frac{\lambda_c}{2}\sqrt{\frac{2}{\varepsilon_r + 1}}, \tag{27}$$

where $\lambda_c = c_0/f_c$. In order to fulfill $f_r = f_c$, the necessary L_{eff} is given in (9). Considering (8), it follows that $L = L_{eff} - 2\Delta L$. Lastly, the necessary x_f is determined, such that $Z_{in} = Z_0$. For $\mu_r = 1$, Z_{in} is given in [41], allowing us to write

$$\begin{aligned} Z_{in} &= \frac{90\varepsilon_r^2 L^2}{(\varepsilon_r - 1)\, W^2}\sin^2\left(\frac{\pi x_f}{L}\right) \Leftrightarrow \\ x_f &= \frac{L}{\pi}\arcsin\left(\sqrt{\frac{Z_{in}(\varepsilon_r - 1)\, W^2}{90L^2\varepsilon_r^2}}\right). \end{aligned} \tag{28}$$

For $f_c = 3.5$ GHz, $Z_{in} = Z_0 = 50\ \Omega$ (see Table 1), along with a substrate such that $\varepsilon_r = 2.55$ and $h = 856.55\ \mu$m, it follows that $W = 32.15$ mm, $L = 25.95$ mm, and $x_f = 3.86$ mm. A low ε_r value is desirable in order to obtain a high radiation efficiency [40], [41]. Accordingly, the Rogers RO4725JXR substrate is chosen, due to its low ε_r and loss tangent, $\tan(\delta^{\text{loss}}) = 2.2 \times 10^{-3}$. The h value previously presented corresponds to $h = \lambda_c/100$. This decision is based on the fact that, in [40], $3\lambda_c/1000 \leq h \leq \lambda_c/20$ is presented as common in microstrip patch antenna design. The theoretical functions $B_{\text{Pm}}^{xz}(\theta)$ and $B_{\text{Pm}}^{yz}(\theta)$, which are the power versions of $B_{\text{Am}}^{xz}(\theta)$ and $B_{\text{Am}}^{yz}(\theta)$, respectively, are shown in Subsection V-A. In general, a given $B_P(\theta, \varphi)$ and the associated $B_A(\theta, \varphi)$ verify $B_P(\theta, \varphi) = B_A^2(\theta, \varphi)$.

C. SUBARRAYS

Isotropic antenna subarrays are considered, since the pattern multiplication theorem (see (12)) shows that the antenna and array sizing can be performed independently. As outlined in Subsection III-D, the isotropic antenna subarrays are defined by specifying M_s, N_s, δ_{xs}, and δ_{ys}. Due to the low f_c value (see Table 1), only $M_s = N_s = 2$ is considered, to minimize the array's area. Furthermore, $\delta_{xs} = \delta_{ys} = \delta_s$ is assumed.

The sizing strategy consists of graphically evaluating the $B_{Ps}(\theta, \varphi) = |\text{AF}_s(\theta, \varphi)|^2$ along the xz plane, denoted by $B_{Ps}^{xz}(\theta, \varphi)$. This is done for antenna spacings δ_s between $0.5\lambda_c$ and λ_c, $\boldsymbol{w}_s(\phi_{xs}, \phi_{ys})$ as defined in (14), and two steering directions, namely $(\varphi_s^{\max}, \theta_s^{\max}) = (0°, 0°)$ and $(\varphi_s^{\max}, \theta_s^{\max}) = (0°, 30°)$. The steering directions chosen are based on the sector coverage (see Table 1). Results along the yz plane are not shown, since, by using isotropic antennas, $B_{Ps}^{xz}(\theta, \varphi)$ steered at $(\varphi_s^{\max}, \theta_s^{\max})$ is equal to $B_{Ps}^{yz}(\theta, \varphi)$ steered at $(\varphi_s^{\max} + 90°, \theta_s^{\max})$.

Fig. 5 shows the $B_{Ps}^{xz}(\theta, \varphi)$, steered at $(\varphi_s^{\max}, \theta_s^{\max}) = (0°, 0°)$ (a) and $(\varphi_s^{\max}, \theta_s^{\max}) = (0°, 30°)$ (b). Note that the elevation values increase along the counterclockwise direction, as indicated by the arrows next to $\theta = 0°$. In both Figs. 5(a) and 5(b), it can be seen that increasing δ_s leads to a narrower main beam, along with more prominent side-lobes. Moreover, the side-lobes in Fig. 5(b) are much more prominent than in Fig. 5(a). It can be noted that grating lobes [41] appear for $\delta_s = \lambda_c$ in Fig. 5(a) and $\delta_s \geq 0.7\lambda_c$ in Fig. 5(b). As a consequence, a spacing $\delta_s = 0.6\lambda_c$ is chosen, which allows for a narrower main beam while avoiding excessively prominent side-lobes.

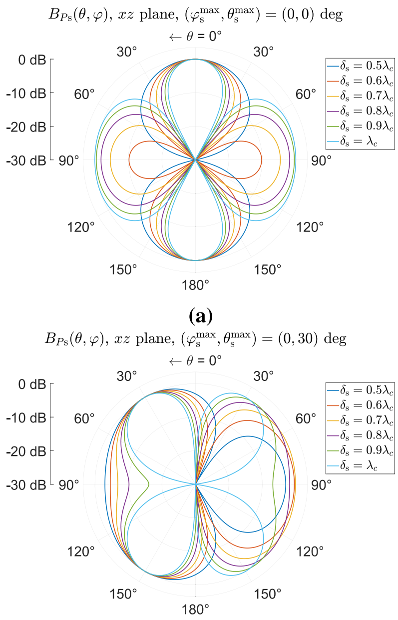

FIGURE 5. Power beam patterns of the isotropic antenna subarrays, in the *xz* plane, for antenna spacingsbetween $0.6\lambda_c$ and λ_c, when steered at broadside (a) and to $(0°, 30°)$ (b).

D. ARRAY

The $M_s = N_s = 2$ and $\delta_s = 0.6\lambda_c$ isotropic antenna subarrays from Subsection IV-C are now the array-level elements. Furthermore, assuming $\delta_{xr} = \delta_{yr} = \delta_r$ leaves δ_r as the only degree of freedom for the array sizing. The array sizing strategy is thus to graphically evaluate the $B_{Pt}(\theta,\varphi) = B_{At}^2(\theta,\varphi)$ along the xz plane, denoted by $B_{Pt}^{xz}(\theta,\varphi)$. This is done for δ_r values between λ_c and $2\lambda_c$, BPS, $\boldsymbol{w}_r(\boldsymbol{A}_r, \phi_r)$ as defined in (19), and two steering directions, $(\varphi^{max}, \theta^{max}) = (0°, 0°)$ and $(\varphi^{max}, \theta^{max}) = (0°, 30°)$. It is assumed that $\varphi_s^{max} = \varphi_r^{max} = \varphi^{max}$ and $\theta_s^{max} = \theta_r^{max} = \theta^{max}$. For brevity, results along the yz plane are not shown. The δ_r values considered take into account that the elements are subarrays, avoiding overlaps.

While the ϕ_r are equal for all scalings, the $\boldsymbol{A}_r$ are not. Since $\boldsymbol{A}_r = \boldsymbol{A}_1/A_c$, the BAS, BPS, and EAS $\boldsymbol{A}_r$ vectors, denoted by $\boldsymbol{A}_r^{BAS}$, $\boldsymbol{A}_r^{BPS}$, and $\boldsymbol{A}_r^{EAS}$, respectively, can be defined analogously to the $\boldsymbol{A}_1^{BAS}$, $\boldsymbol{A}_1^{BPS}$, and $\boldsymbol{A}_1^{EAS}$ in (6), resulting in

$$\begin{aligned}\boldsymbol{A}_r^{BAS} &= \left[\frac{A_r^{BAS,ref}}{8}\ \frac{A_r^{BAS,ref}}{4}\ \frac{A_r^{BAS,ref}}{2}\ A_r^{BAS,ref}\right]^T,\\ \boldsymbol{A}_r^{BPS} &= \left[\frac{A_r^{BPS,ref}}{2\sqrt{2}}\ \frac{A_r^{BPS,ref}}{2}\ \frac{A_r^{BPS,ref}}{\sqrt{2}}\ A_r^{BPS,ref}\right]^T,\\ \boldsymbol{A}_r^{EAS} &= \left[A_r^{EAS,ref}\ A_r^{EAS,ref}\ A_r^{EAS,ref}\ A_r^{EAS,ref}\right]^T,\end{aligned} \tag{29}$$

where $A_r^{BAS,ref}$, $A_r^{BPS,ref}$, and $A_r^{EAS,ref}$ are the reference amplitude values for BAS, BPS, and EAS, respectively. All A_{1b} under EAS verify $A_{1b} = A_c$, thus, $A_r^{EAS,ref} = 1$. The $A_r^{BAS,ref}$ and $A_r^{BPS,ref}$ values are defined such that $\|\boldsymbol{A}_r^{BAS}\|^2 = \|\boldsymbol{A}_r^{BPS}\|^2 = \|\boldsymbol{A}_r^{EAS}\|^2$, resulting in $A_r^{BAS,ref} = (8/85)\sqrt{85}\|\boldsymbol{A}_r^{EAS}\|$ and $A_r^{BPS,ref} = (2/15)\sqrt{30}\|\boldsymbol{A}_r^{EAS}\|$.

Fig. 6 shows the resulting $B_{Pt}^{xz}(\theta,\varphi)$ for BPS, steered at $(\varphi^{max}, \theta^{max}) = (0°, 0°)$ (a) and $(\varphi^{max}, \theta^{max}) = (0°, 30°)$ (b). In both Figs. 6(a) and 6(b), it can be seen that increasing δ_r always leads to a narrower main beam. However, the side-lobes no longer become monotonically more prominent by increasing δ_r. Moreover, the side-lobes are much more prominent in Fig. 6(b) than in Fig. 6(a). It can be noted that grating lobes are no longer verified, in any of the cases. Consequently, the spacing $\delta_r = 1.2\lambda_c$ is chosen, allowing for a slightly narrower main beam in Figs. 6(a) and 6(b), along with less prominent side-lobes in Fig. 6(a), when compared to $\delta_r = \lambda_c$.

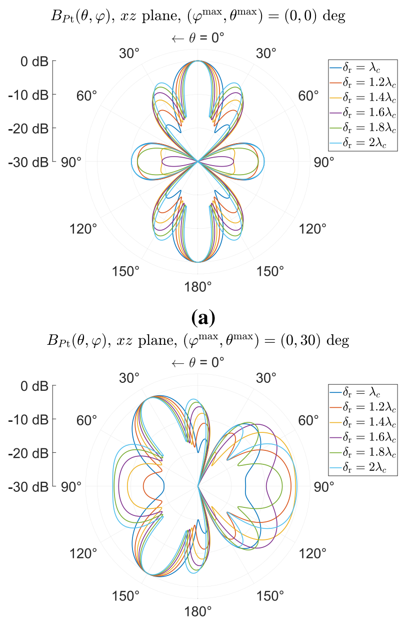

FIGURE 6. Power beam patterns for arrays with 2×2, $0.6\lambda_c$-spaced isotropic antenna subarrays, in the *xz* plane, for BPS, subarray spacings between λ_c and $2\lambda_c$, when steered at broadside (a) and to $(0°, 30°)$ (b).

V. MODELING AND SIMULATION

In this section, the microstrip patch antennas, array, and PCOA system are modeled and simulated, in Subsections V-A, V-B, and V-C, respectively. Based on the simulated results, the initial sizings are adjusted, in order to meet the specified goals.

A. MICROSTRIP PATCH ANTENNAS

The MATLAB™ Antenna Designer is used to model and simulate the rectangular microstrip patch antennas. The initial sizing consists of the values outlined in Subsection IV-B, along with $h_c = 35.56$ μm, $\sigma = 5.96 \times 10^7$ S/m, and $W_g = L_g = \lambda_c = 85.66$ mm. All subsequent microstrip patch antenna and array models assume that the substrate has the same width and length as the ground plane.

Fig. 7 shows the theoretical and simulated power beam patterns $B_{Pm}^{xz}(\theta, \varphi)$ (a) and $B_{Pm}^{yz}(\theta, \varphi)$ (b). It can be seen that the simulated (initial sizing) and theoretical results differ, especially for θ values which are substantially different from $\theta = 0^\circ$. This discrepancy is expected, since the theoretical analysis assumes $W_g = L_g = \infty$ m [41].

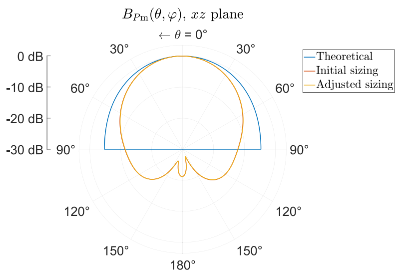

(a)

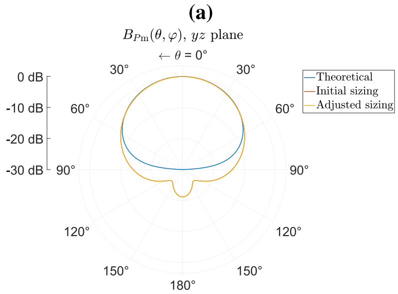

(b)

FIGURE 7. Theoretical and simulated power beam patterns for the microstrip patch antenna, in the *xz* (a) and *yz* (b) planes.

Fig. 8 shows the S-parameter $|S_{1,1}|$ for the initial and adjusted microstrip patch antenna sizings. It can be seen that the initial sizing results in an f_r which is very close to f_c. However, at f_c, the input reflection coefficient is $|S_{1,1}| = -14.83$ dB. Although this value might be acceptable, in this work, we consider that good match is defined as $|S_{n,n}| < -20$ dB.

This means that the microstrip patch antenna sizing needs to be adjusted. Accordingly, L and x_f are altered, such that $L = 25.97$ mm and $x_f = 4.75$ mm. It can be seen in Fig. 7 that the initial and adjusted designs results in very similar beam patterns. More importantly, the simulated $|S_{1,1}|$ with the adjusted sizing, shown in Fig. 8, now verifies $|S_{1,1}| = -46.47$ dB at f_c.

A given $B_{Pm}^{xz}(\theta, \varphi)$ relates to the gain function $G_{m}^{xz}(\theta, \varphi)$ through $G_{m}^{xz}(\theta, \varphi) = G_{0m}^{xz} B_{Pm}^{xz}(\theta, \varphi)$ [41], where G_{0m}^{xz} is the

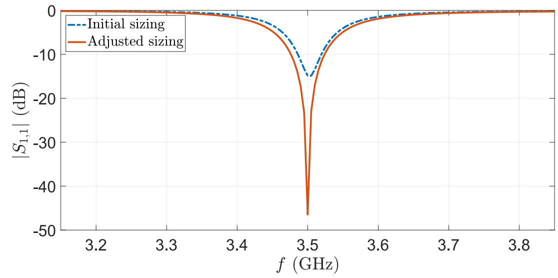

FIGURE 8. Simulated input reflection coefficient of the microstrip patch antenna, for the initial and adjusted sizings.

maximum gain in the xz plane. Analogously, $G_{m}^{yz}(\theta, \varphi) = G_{0m}^{yz} B_{Pm}^{yz}(\theta, \varphi)$, where G_{0m}^{yz} is the maximum gain in the yz plane. The initially sized microstrip patch antenna verifies $G_{0m}^{xz} = 6.95$ dBi, achieved at $\theta = 2^\circ$, $G_{0m}^{yz} = 6.94$ dBi, achieved at $\theta = 0^\circ$, and presents a radiation efficiency, η_{m}^{rad}, of 77.36%. The microstrip patch antenna with the adjusted sizing verifies $G_{0m}^{xz} = 6.94$ dBi, achieved at $\theta = 1^\circ$, $G_{0m}^{yz} = 6.93$ dBi, achieved at $\theta = 0^\circ$, and $\eta_{m}^{rad} = 77.05\%$.

B. ARRAY

For brevity, the array-level results only consider the xz plane. The MATLAB™ Antenna Array Designer is used to model and simulate the rectangular microstrip patch antenna arrays. The initial array design considers $W_{gt} = L_{gt} = 342.62$ mm, where W_{gt} and L_{gt} are the array's ground plane width and length, along with the adjusted microstrip patch antenna, designed in Subsection V-A. For the initial antenna spacing, δ, it follows that $\delta = 51.39$ mm when considering the δ_s and δ_r sizings, in Subsections IV-C and IV-D, respectively.

Fig. 9 shows the simulated S-parameters, for the initial (a) and adjusted (b) array sizing, considering BPS and steering

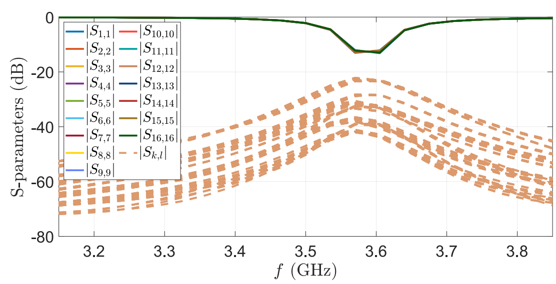

(a)

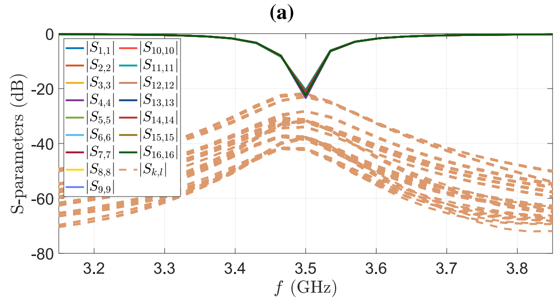

(b)

FIGURE 9. Simulated S-parameters for the initial (a) and adjusted (b) array sizing, considering BPS and steering at broadside.

at $(\varphi^{\max}, \theta^{\max}) = (0^\circ, 0^\circ)$. The notation $|S_{k,l}|$ denotes the S-parameter from the lth to the kth antenna, where $k = \{1, 2, \ldots, 16\}$, $l = \{1, 2, \ldots, 16\}$. The antenna index k relates to the (m, n) notation presented in Fig. 3 through $m = \text{floor}((k-1)/4)+1$, $n = 4-((k-1) \bmod 4)$, where mod is the modulo operation. The antenna index l follows analogously. A total of 256 S-parameters exist, 16 of which are of the form $|S_{k,k}|$, representing input reflection coefficients, and the remaining 240 $|S_{k,l}|$, with $k \neq l$, represent interactions between the antennas through mutual coupling [40], [41]. It can be seen in Fig. 9(a) that the array-level f_r deviates from f_c, and that $\min(|S_{k,k}|) = -13.18$ dB, deviating significantly from the adjusted microstrip patch antenna results in Subsection V-A. By adjusting the L and x_f for all antennas to $L = 26.69$ mm and $x_f = 5$ mm, respectively, the resulting S-parameters are shown in Fig. 9(b), where $f_r = f_c$ is now verified. Furthermore, $\min(|S_{k,k}|) = -23.47$ dB at f_c, and $\max(|S_{k,k}|) = -20.49$ dB at f_c, representing a good match.

Fig. 10 shows the simulated array gain functions $G_{\mathrm{t}}(\theta, \varphi)$ in the xz plane, $G_{\mathrm{t}}^{xz}(\theta, \varphi)$, when steered at $(\varphi^{\max}, \theta^{\max}) = (0^\circ, 0^\circ)$ (a) and $(\varphi^{\max}, \theta^{\max}) = (0^\circ, 30^\circ)$ (b), considering BAS, BPS, and EAS. From this figure, it can be seen that the results with the initial and adjusted designs are very similar. Denoting the gain at $(\varphi^{\max}, \theta^{\max})$ as $G_{\mathrm{t}}^{\text{steering}}$, it is shown in (a) and (b) that EAS is the best option, always offering the highest $G_{\mathrm{t}}^{\text{steering}}$, followed by BPS, with BAS always offering the lowest value. It can also be noted that grating lobes are not present in any configuration. In Fig. 10(b), it can be seen that the maximum gain values are not achieved at $(\varphi^{\max}, \theta^{\max}) = (0^\circ, 30^\circ)$. This is due to the behavior of the microstrip patch antenna xz-plane power beam pattern, $B_{P\mathrm{m}}^{xz}(\theta, \varphi)$, which introduces attenuation outside of $(\varphi, \theta) = (0^\circ, 0^\circ)$, as can be seen in Fig. 7(a).

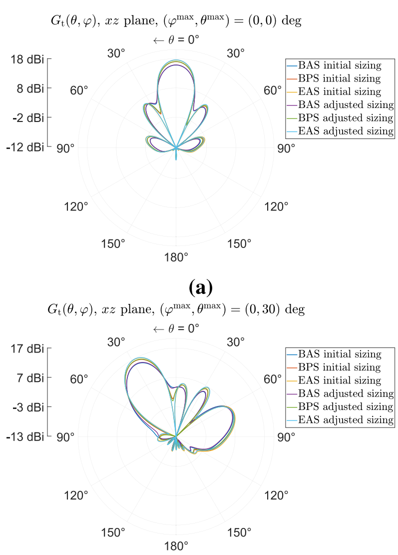

FIGURE 10. Simulated gain functions for the arrays, in the *xz* plane, for BAS, BPS, and EAS, when steered at broadside (a) and to (0°, 30°) (b).

The array radiation efficiency, $\eta_{\mathrm{t}}^{\text{rad}}$, is estimated through $\eta_{\mathrm{t}}^{\text{rad}} = G_{\mathrm{t}}(\theta, \varphi)/(D_{\mathrm{t}}(\theta, \varphi))$ [41], where $D_{\mathrm{t}}(\theta, \varphi)$ is the array directivity function. The initially sized array, when steered at $(\varphi^{\max}, \theta^{\max}) = (0^\circ, 0^\circ)$, presents $\eta_{\mathrm{t}}^{\text{rad}}$ values of 78.34%, 78.67%, and 78.86%, for BAS, BPS, and EAS, respectively. For steering at $(\varphi^{\max}, \theta^{\max}) = (0^\circ, 30^\circ)$, $\eta_{\mathrm{t}}^{\text{rad}}$ values of 81.25%, 81.13%, and 81.10% are obtained, for BAS, BPS, and EAS, respectively. With the adjusted sizing, $\eta_{\mathrm{t}}^{\text{rad}}$ values of 79.15%, 79.49%, and 79.68%, are obtained, for BAS, BPS, and EAS, respectively, when steered at $(\varphi^{\max}, \theta^{\max}) = (0^\circ, 0^\circ)$. For steering at $(\varphi^{\max}, \theta^{\max}) = (0^\circ, 30^\circ)$, $\eta_{\mathrm{t}}^{\text{rad}}$ values of 81.42%, 81.34%, and 81.35% are obtained, for BAS, BPS, and EAS, respectively.

C. PCOA SYSTEM

The architecture in Fig. 1 is implemented in the MATLAB™ Simulink environment. Similarly to Subsection V-B, the PCOA-level results only consider the xz plane. Whenever applicable, $Z_{in} = Z_{out} = Z_0 = 50\ \Omega$ is followed, and the noise modeling considers a temperature of 300 K (26.85 °C).

All input signals $s_b(t)$ verify $\vartheta_b = 0^\circ$ and their amplitudes are set based on the P_{sb} values in Table 2. The coefficients of the SMPA nonlinear functions $p_b(\cdot)$ are the ones specified in Table 2, where the G_{pb}^{ideal} values are interpreted as available gain. SMPA-level noise modeling is considered, with a noise figure (NF) of 3 dB. The BPFs are modeled as T networks, with the $H_b(f)$ being second-order Butterworth ($\epsilon = 1$) transfer functions, centered at $f_c = 3.5$ GHz, with a bandwidth of 100 MHz. All PCOA insertion losses are modeled by introducing 1 dB of insertion loss to each $u_b(t)$ signal. The uniform splitters are assumed to be ideal Wilkinson power dividers, with a reference impedance of $Z_0 = 50\ \Omega$. The adjusted array model in Subsection V-B is imported as the transmitting array, with noise modeling being considered. For the channel, $\beta = (\lambda_c/(4\pi d))^2$ [43], where d is the distance between the transmitter and receiver, and a noise power spectral density (PSD) of -160 dBm/Hz (10^{-19} W/Hz) are considered. The adjusted microstrip patch antenna model in Subsection V-A is imported as the receiver antenna, with noise modeling also being considered. Thus, the array and receive microstrip patch antennas are linearly polarized [41]. Furthermore, their models are based on full-wave electromagnetic analysis. Perfect receiver-level alignment is always assumed.

Table 3 shows the simulated P_{yb}, P_y^{total}, and effective isotropic radiated power (EIRP) values at the steering direction, EIRP$(\theta^{\max}, \varphi^{\max})$, for the three scalings, the initial and adjusted SMPAs, along with steering at $(\varphi^{\max}, \theta^{\max}) = (0^\circ, 0^\circ)$ and $(\varphi^{\max}, \theta^{\max}) = (0^\circ, 30^\circ)$. The initial simulations consider the P_{IIP3} values in Table 2, and are only presented for $(\varphi^{\max}, \theta^{\max}) = (0^\circ, 0^\circ)$. From these, it can be seen that the P_{yb} values never follow the scaling definitions in (24). The error is significant for BAS and BPS, and slight for EAS. Furthermore, all scalings deviate from the intended total SMPA output power at f_c, $P_y^{\text{total}} = 30$ dBm (see Table 1). This is attributed to the fact that mutual

TABLE 3. Simulated per-branch SMPA fundamental frequency output powers, total SMPA output power, and EIRP at the steering direction for PCOA under BAS, BPS, and EAS, the initial and adjusted IIP3 values, when steered at broadside and to (0°, 30°).

Configuration	$(\varphi^{max}, \theta^{max})$ (°)	P_{y1} (dBm)	P_{y2} (dBm)	P_{y3} (dBm)	P_{y4} (dBm)	P_y^{total} (dBm)	EIRP$(\theta^{max}, \varphi^{max})$ (dBm)
BAS initial	(0,0)	11.06	17.05	22.64	28.64	29.90	44.77
BPS initial	(0,0)	18.34	21.34	24.17	27.17	29.94	45.98
EAS initial	(0,0)	23.95	23.95	23.94	23.95	29.97	46.57
BAS adjusted	(0,0)	10.71	16.73	22.75	28.77	30	44.8
BPS adjusted	(0,0)	18.24	21.25	24.26	27.27	30	46.01
EAS adjusted	(0,0)	23.98	23.98	23.98	23.98	30	46.59
BAS adjusted	(0,30)	11.80	17.39	23.09	29.36	30.56	44.05
BPS adjusted	(0,30)	18.92	21.84	24.71	27.82	30.54	45.22
EAS adjusted	(0,30)	24.55	24.49	24.53	24.49	30.54	45.78

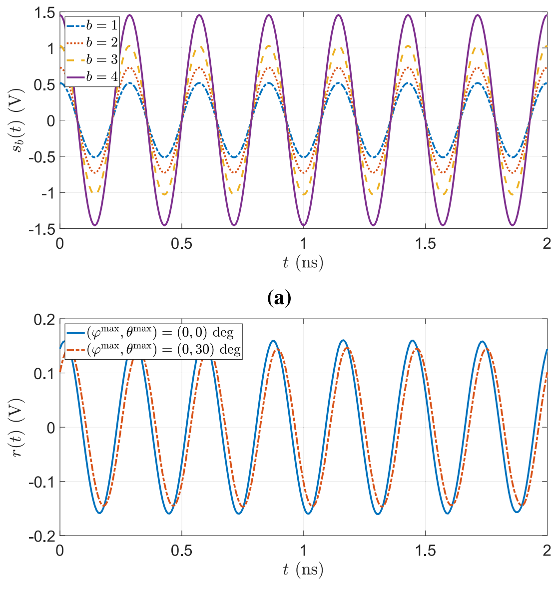

FIGURE 11. Simulated input signals (a) and received signals (b) in the time domain, for PCOA under BPS and a distance of 6 m, when steered atbroadside and to (0°, 30°).

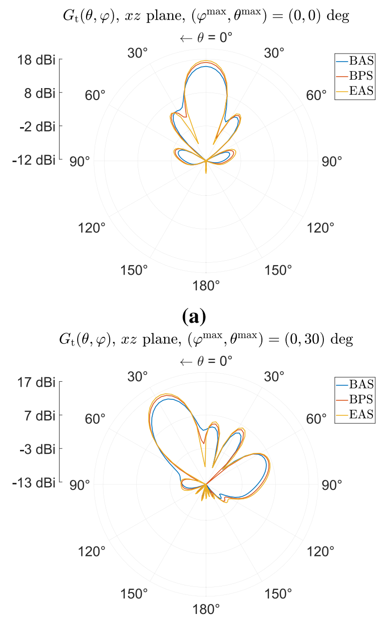

FIGURE 12. Simulated gain functions for the array, in the *xz* plane, for PCOA under BAS, BPS, and EAS, when steered at broadside (a) and to (0°, 30°) (b).

coupling influences the active Z_{in} associated to the array's antennas [41]. Accordingly, the SMPA sizings (P_{IIP3b} values) are adjusted such that (24) and $P_y^{total} = 30$ dBm are simultaneously verified for $(\varphi^{max}, \theta^{max}) = (0°, 0°)$.

Denoting as $\boldsymbol{P}_{IIP3} \in \mathbb{R}^{4\times1}$ the vector containing the P_{IIP3b} values, it follows that $\boldsymbol{P}_{IIP3}^{BAS}$, $\boldsymbol{P}_{IIP3}^{BPS}$, and $\boldsymbol{P}_{IIP3}^{EAS}$ are the $\boldsymbol{P}_{IIP3}$ for BAS, BPS, and EAS, respectively. The adjusted P_{IIP3b} values can thus be expressed as $\boldsymbol{P}_{IIP3}^{BAS} = [2.91 \;\; 8.98 \;\; 15.84 \;\; 21.91]^T$ dBm, for BAS, $\boldsymbol{P}_{IIP3}^{BPS} = [10.91 \; 13.94 \; 17.30 \; 20.33]^T$ dBm, for BPS, and $\boldsymbol{P}_{IIP3}^{EAS} = [16.91 \;\; 16.90 \;\; 16.91 \;\; 16.91]^T$ dBm, for EAS, respectively. Considering these values, Table 3 shows that for $(\varphi^{max}, \theta^{max}) = (0°, 0°)$, (24) and $P_y^{total} = 30$ dBm are both, in fact, verified, for all scalings. However, the results deviate once again for $(\varphi^{max}, \theta^{max}) = (0°, 30°)$, since the antenna-level active Z_{in} values depend on the applied phase shifts [41]. Considering the adjusted results, it can be seen that from $(\varphi^{max}, \theta^{max}) = (0°, 0°)$ to $(\varphi^{max}, \theta^{max}) = (0°, 30°)$, the EIRP values decrease and the P_y^{total} values increase, representing a decrease in the system-level efficiency. Unless stated otherwise, the P_{sb} values presented in Table 2 are considered for the following PCOA simulations.

Fig. 11 shows the input signals $s_b(t)$ (a) and the corresponding received signals $r(t)$ (b) for BPS, $d = 6$ m, when steered at $(\varphi^{max}, \theta^{max}) = (0°, 0°)$ and $(\varphi^{max}, \theta^{max}) = (0°, 30°)$. The distance is chosen such $d > d_{FF}$, where d_{FF} is the Fraunhofer distance, given by $d_{FF} = (2/\lambda_c)D_a^2$ [41], with D_a being the largest dimension of the antenna structure. Considering the W_{gt} and L_{gt} values in Subsection V-B, it follows that $d_{FF} = 5.48$ m. The $s_b(t)$ signals do not depend on $(\varphi^{max}, \theta^{max})$, thus, only one set is presented in Fig. 11(a). In Fig. 11(b), it can be seen that the PCOA process is correctly performed, by the reception of one distortion-free sinusoidal signal, for each steering scenario. Considering the EIRP values in Table 3, $d = 6$ m, and the receiver microstrip patch antenna gain in the xz plane of 6.93 dBi for $\theta = 0°$, the predicted and simulated $r(t)$ signal power, P_r, can be compared. For $(\varphi^{max}, \theta^{max}) = (0°, 0°)$ $P_r = -5.95$ dBm is predicted, and $P_r = -5.96$ dBm is measured. For $(\varphi^{max}, \theta^{max}) = (0°, 30°)$, $P_r = -6.74$ dBm

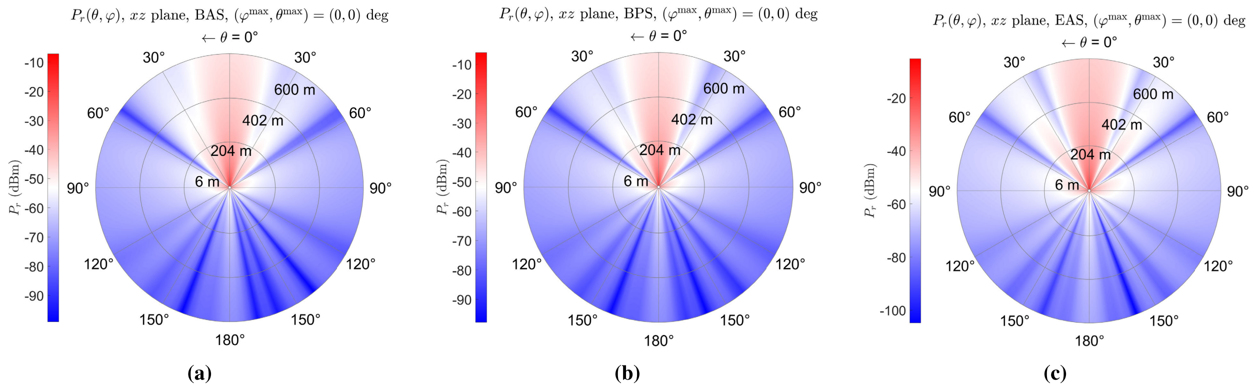

FIGURE 13. Simulated RX power heatmaps for PCOA under BAS (a), BPS (b), and EAS (c), in the *xz* plane, considering distances from 6 m to 600 m, when steered at broadside.

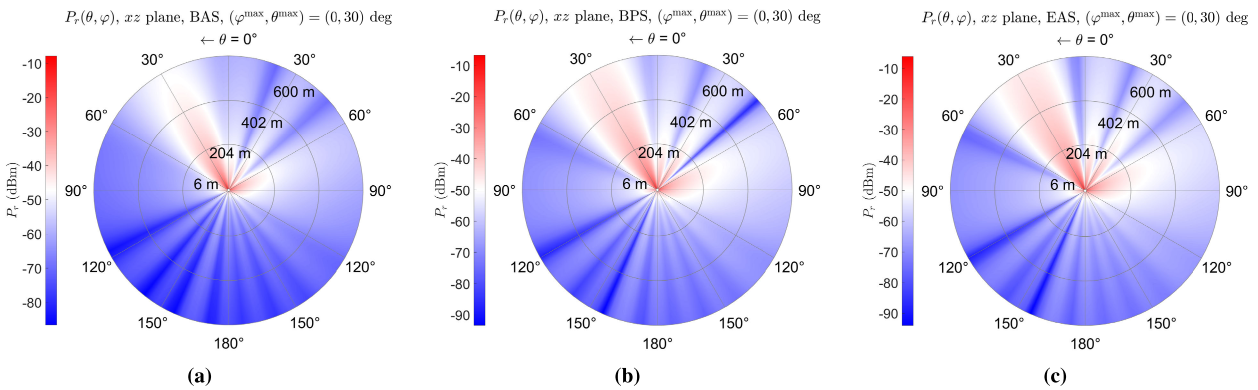

FIGURE 14. Simulated RX power heatmaps for PCOA under BAS (a), BPS (b), and EAS (c), in the *xz* plane, considering distances from 6 m to 600 m, when steered to $(0^\circ, 30^\circ)$.

is predicted, and $P_r = -6.75$ dBm is measured. Both sets of P_r values validate the OTA combination performed in PCOA.

Fig. 12 shows the simulated PCOA xz-plane array gain function $G_t^{xz}(\theta, \varphi)$, for BAS, BPS, and EAS, when steered at $(\varphi^{\max}, \theta^{\max}) = (0^\circ, 0^\circ)$ (a) and $(\varphi^{\max}, \theta^{\max}) = (0^\circ, 30^\circ)$ (b). The same conclusions hold as for Fig. 10, since the results are very similar.

Figs. 13 and 14 present the xz-plane received power heatmaps, denoted by $P_r^{xz}(\theta, \varphi)$, for BAS (a), BPS (b), and EAS (c), $d = 6$ m to $d = 600$ m, when steered at $(\varphi^{\max}, \theta^{\max}) = (0^\circ, 0^\circ)$ and $(\varphi^{\max}, \theta^{\max}) = (0^\circ, 30^\circ)$, respectively. In all cases, it can be seen that the power is mostly concentrated in the main beam, and rapidly decreases with misalignment, distance, or both. Thus, very little inference is presented to neighboring systems. Combined with the high array radiation efficiency values (see Subsection V-B), we can conclude that the proposed PCOA technique excels at efficiently directing the intended signal power to the receiver.

Lastly, while the presented PCOA system is shown to correctly and efficiently perform the OTA combination of the components, it is also shown in Table 3 that adjusting the SMPAs for $(\varphi^{\max}, \theta^{\max}) = (0^\circ, 0^\circ)$ is insufficient to mitigate the per-branch RF power variations when the transmission is steered to other directions (due to mutual coupling). As such, a compensation strategy is presented, which is able to simultaneously fulfill (24) and $P_y^{\text{total}} = 30$ dBm, across the full sector.

The proposed compensation strategy is, for each steering direction within a discrete set, to calibrate the input power values, P_{sb}, such that (24) and $P_y^{\text{total}} = 30$ dBm are once again verified. The key reason for discretizing the steering directions is that the resulting compensation has a very low complexity, since the calibrated input power values can then be stored in lookup tables (LUTs). With this approach, the P_{sb} values do change according to the steering direction. However, they remain constant for a given direction.

For the steering directions given by $\varphi^{\max} = 0^\circ \vee \varphi^{\max} = 180^\circ$, $\theta^{\max} = \{0^\circ, 3^\circ, \ldots, 30^\circ\}$ (thus within the xz plane), the difference between the uncompensated and compensated $\text{EIRP}(\theta^{\max}, \varphi^{\max})$ values (in dBm) is determined, denoted by $\Delta\text{EIRP}(\theta^{\max}, \varphi^{\max})$. Similarly, the difference between the uncompensated and compensated $G_t(\theta^{\max}, \varphi^{\max})$ values (in dB) is determined, denoted by $\Delta G_t(\theta^{\max}, \varphi^{\max})$.

Fig. 15 presents the resulting $\Delta\text{EIRP}(\theta^{\max}, \varphi^{\max})$ and $\Delta G_t(\theta^{\max}, \varphi^{\max})$ values, for BPS and the aforementioned 21 steering directions. It can be noted that both the $\Delta\text{EIRP}(\theta^{\max}, \varphi^{\max})$ and $\Delta G_t(\theta^{\max}, \varphi^{\max})$ values are small, with the $\Delta G_t(\theta^{\max}, \varphi^{\max})$ values in particular being extremely small. Thus, the most impactful consequence of mutual coupling within PCOA is the alteration of the total SMPA output power, the scaling distortion plays a very minor role.

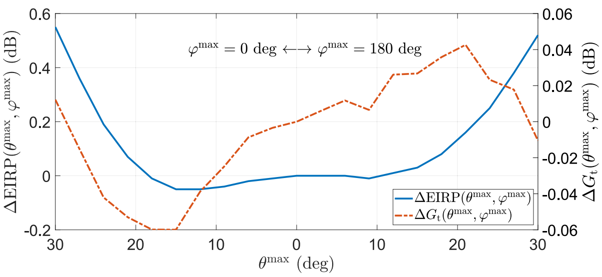

FIGURE 15. **Simulated difference between the uncompensated and compensated EIRP values, along with the difference between the uncompensated and compensated array gain values, for PCOA under BPS, and the 21 steering directions within the sector.**

VI. CONCLUSION

In this work, we further explored the multi-branch PCOA transmitter architecture, where three different scalings were considered for the branches. The proposed OTA combination helps minimize the circuit-based power combiner insertion losses, and the constant-envelope components allow us to use highly-efficient SMPAs. We theoretically analyze and design the different PCOA blocks, present optimized SMPA (at the system level) and array sizings, and explore detailed microstrip patch antenna and array modeling, with a comercially available substrate and copper as the conductor.

For all scalings, it is shown that the proposed PCOA system correctly and efficiently combines the different sinusoidal components, to any steering direction within the sector. Notable points include the introduction of array gain, very low interference to neighbouring systems, and the architectural minimization of insertion losses. The final array presents η_t^{rad} values as high as 81.42%, and $|S_{n,n}| < -20$ dB is verified for all antennas. Importantly, the array and SMPA sizings in the PCOA system need to take into account the impact of mutual coupling between the array antennas. Despite the sizing adjustments, it is shown that steering the transmission through the applied phase shifts decreases the system-level efficiency and can distort the RF-level branch powers. However, a low-complexity, simple compensation strategy is presented, which shows the that mutual coupling effects have a small impact.

From the different scalings, EAS is shown to result in the best array-level performance, closely followed by BPS, with BAS being significantly more disadvantageous than both. Thus, future works evaluating the EAS and BPS PCOA system with a signal decomposition scheme, along with addressing memory effects and the beam squinting phenomenon in wideband contexts are key steps toward a complete, next-generation compliant transmitter architecture that can feature a high EE.

REFERENCES

[1] E. Kolta and T. Hatt. (Feb. 2024). *Going Green: Measuring the Energy Efficiency of Mobile Networks*. [Online]. Available: https://www.gsmaintelligence.com/research/going-green-measuring-the-energy-efficiency-of-mobile-networks

[2] L. Sboui, Z. Rezki, A. Sultan, and M.-S. Alouini, "A new relation between energy efficiency and spectral efficiency in wireless communications systems," *IEEE Wireless Commun.*, vol. 26, no. 3, pp. 168–174, Jun. 2019.

[3] T. S. Rappaport, M. Ying, N. Piovesan, A. De Domenico, and D. Shakya, "Waste factor and waste figure: A unified theory for modeling and analyzing wasted power in radio access networks for improved sustainability," *IEEE Open J. Commun. Soc.*, vol. 5, pp. 4839–4867, 2024.

[4] *3rd Generation Partnership Project; Technical Specification Group Radio Access Network; Evolved Universal Terrestrial Radio Access (E-UTRA); LTE Physical Layer; General Description (Release 19)*, document TS 36.201 V19.0.0, 3GPP, Sep. 2025.

[5] *Technical Specification Group Radio Access Network; NR; Physical Layer; General Description (Release 19)*, document TS 38.201 V19.0.0, 3rd Generation Partnership Project, Jun. 2025.

[6] Mobile Competence Centre, *Final Report of 3GPP TSG RAN WG1 #122 V1.0.0 (bengaluru, India, August 25th-29th, 2025)*, document R1-2506702, Oct. 2025. [Online]. Available: https://www.3gpp.org/ftp/tsg_ran/wg1_rl1/TSGR1_

[7] Y. Rahmatallah and S. Mohan, "Peak-to-average power ratio reduction in OFDM systems: A survey and taxonomy," *IEEE Commun. Surveys Tuts.*, vol. 15, no. 4, pp. 1567–1592, Dec. 2013.

[8] A. Kakkavas, W. Xu, J. Luo, M. Castañeda, and J. A. Nossek, "On PAPR characteristics of DFT-s-OFDM with geometric and probabilistic constellation shaping," in *Proc. IEEE 18th Int. Workshop Signal Process. Adv. Wireless Commun. (SPAWC)*, Jul. 2017, pp. 1–5.

[9] M. K. Kazimierczuk, *RF Power Amplifiers*, 2nd ed., Hoboken, NJ, USA: Wiley, 2015.

[10] F. Conceição, M. Gomes, V. Silva, R. Dinis, A. Silva, and D. Castanheira, "A survey of candidate waveforms for beyond 5G systems," *Electron.*, vol. 10, no. 1, pp. 1–26, Dec. 2020.

[11] M. Diacu, J. P. Oliveira, and J. Guerreiro, "The case for switched-mode transmitter architectures in efficient 5G/6G mobile networks based on power amplifier survey," in *Proc. 2025 9th Int. Young Engineers Forum Elect. Comput. Eng. (YEF-ECE)*, Portugal, Jul. 2025, pp. 180–185.

[12] V. Camarchia, M. Pirola, R. Quaglia, S. Jee, Y. Cho, and B. Kim, "The Doherty power amplifier: Review of recent solutions and trends," *IEEE Trans. Microw. Theory Techn.*, vol. 63, no. 2, pp. 559–571, Feb. 2015.

[13] J. Moon, J. Kim, J. Kim, I. Kim, and B. Kim, "Efficiency enhancement of Doherty amplifier through mitigation of the knee voltage effect," *IEEE Trans. Microw. Theory Techn.*, vol. 59, no. 1, pp. 143–152, Jan. 2011.

[14] J. Xia, X. Zhu, L. Zhang, J. Zhai, and Y. Sun, "High-efficiency GaN Doherty power amplifier for 100-MHz LTE-advanced application based on modified load modulation network," *IEEE Trans. Microw. Theory Techn.*, vol. 61, no. 8, pp. 2911–2921, Aug. 2013.

[15] T. Barton, "Not just a phase: Outphasing power amplifiers," *IEEE Microw. Mag.*, vol. 17, no. 2, pp. 18–31, Feb. 2016.

[16] A. Banerjee, L. Ding, and R. Hezar, "A high efficiency multi-mode outphasing RF power amplifier with 31.6 dBm peak output power in 45nm CMOS," *IEEE Trans. Circuits Syst. I, Reg. Papers*, vol. 67, no. 3, pp. 815–828, Mar. 2020.

[17] P. A. Godoy, S. Chung, T. W. Barton, D. J. Perreault, and J. L. Dawson, "A 2.4-GHz, 27-dBm asymmetric multilevel outphasing power amplifier in 65-nm CMOS," *IEEE J. Solid-State Circuits*, vol. 47, no. 10, pp. 2372–2384, Oct. 2012.

[18] P. Viegas, "Amplificação linear quantizada de sinais multi-portadora," M.S. thesis, Dept. Elect. and Comput. Eng., Univ. NOVA de Lisboa, Caparica, Portugal, 2017.

[19] P. Montezuma, R. Madeira, H. Serra, P. Viegas, R. Dinis, J. Oliveira, and J. Guerreiro, "Quantized digital amplification with combination over the air–achieving maximum efficiency on communication links between long range UAVs and satellites," in *Proc. IEEE Mil. Commun. Conf. (MILCOM)*, San Diego, CA, USA, Nov. 2021, pp. 802–807.

[20] P. Viegas, H. Serra, J. Guerreiro, R. Madeira, D. Borges, R. Dinis, P. Montezuma, J. P. Oliveira, L. M. Campos, and M. Beko, "A novel highly-efficient amplification scheme for wireless communications in a CathLab environment," *IEEE Access*, vol. 9, pp. 87520–87530, 2021.

[21] P. Montezuma, D. Marques, V. Astucia, R. Dinis, and M. Beko, "Robust frequency-domain receivers for a transmission technique with directivity at the constellation level," in *Proc. IEEE 80th Veh. Technol. Conf. (VTC-Fall)*, Vancouver, BC, Canada, Sep. 2014, pp. 1–7.

[22] V. Lampu, G. Xu, A. Brihuega, M. Kosunen, V. Unnikrishnan, J. Ryynänen, C. Fager, M. Valkama, and L. Anttila, "Multilevel outphasing with over-the-air combining in large antenna arrays," *IEEE Trans. Commun.*, vol. 71, no. 12, pp. 7347–7362, Dec. 2023.

[23] B. Kim, J. Kim, D. Kim, J. Son, Y. Cho, J. Kim, and B. Park, "Push the envelope: Design concepts for envelope-tracking power amplifiers," *IEEE Microw. Mag.*, vol. 14, no. 3, pp. 68–81, May 2013.

[24] L. Anttila, V. Toivonen, O. Tervo, E. Tiirola, K. Hooli, J. Talvitie, and M. Valkama, "Feasibility of DFT-s-OFDM in 6G downlink: Coverage and energy-efficiency assessment," in *Proc. Joint Eur. Conf. Netw. Commun. 6G Summit (EuCNC/6G Summit)*, Antwerp, Belgium, Jun. 2024, pp. 1–6.

[25] J. Guerreiro, R. Dinis, P. Montezuma, J. P. Oliveira, and M. Silva, "A multi-branch linear amplification with nonlinear components technique," in *Proc. IEEE Mil. Commun. Conf. (MILCOM)*, Oct. 2018, pp. 1–5.

[26] M. Diacu, J. Guerreiro, J. P. Oliveira, P. Montezuma, and P. Viegas, "High-level modeling of RF power amplifiers and antenna arrays for efficient over-the-air power combination in RF transceivers," in *Proc. 32nd Int. Conf. Mixed Design Integr. Circuits Syst. (MIXDES)*, Jun. 2025, pp. 150–155.

[27] *3rd Generation Partnership Project; Technical Specification Group Radio Access Network; NR; Base Station (BS) Radio Transmission and Reception (Release 19)*, document TS 38.104 V19.2.0, Sep. 2025.

[28] *3rd Generation Partnership Project; Technical Specification Group Radio Access Network; Study on Scenarios and Requirements for Next Generation Access Technologies; (release 19)*, document TR 38.913, Sep. 2025.

[29] A. E. Martynyuk, A. G. Martinez-Lopez, and J. I. Martinez Lopez, "2-bit X-band reflective waveguide phase shifter with BCB-based bias circuits," *IEEE Trans. Microw. Theory Techn.*, vol. 54, no. 12, pp. 4056–4061, Dec. 2006.

[30] A. Malczewski, S. Eshelman, B. Pillans, J. Ehmke, and C. L. Goldsmith, "X-band RF MEMS phase shifters for phased array applications," *IEEE Microw. Guided Wave Lett.*, vol. 9, no. 12, pp. 517–519, Dec. 1999.

[31] F. Liu, J. Xu, Y.-W. Duan, H. Wan, H. Zhang, and L. Zhu, "A 5-bit digital phase shifter using phase-tuning property of open-/short-circuit microstrip line-loaded slot line structure," *IEEE Trans. Microw. Theory Techn.*, vol. 71, no. 6, pp. 2606–2615, Jun. 2023.

[32] K. H. An, O. Lee, H. Kim, D. H. Lee, J. Han, and K. S. Yang, Y. Kim, J. J. Chang, W. Woo, C.-H. Lee, H. Kim, and J. Laskar, "Power-combining transformer techniques for fully-integrated CMOS power amplifiers," *IEEE J. Solid-State Circuits*, vol. 43, no. 5, pp. 1064–1075, May 2008.

[33] S. B. Cohn, "A class of broadband three-port TEM-mode hybrids," *IEEE Trans. Microw. Theory Techn.*, vol. MTT-16, no. 2, pp. 110–116, Feb. 1968.

[34] A. Wentzel, V. Subramanian, A. Sayed, and G. Boeck, "Novel broadband Wilkinson power combiner," in *Proc. Eur. Microw. Conf.*, Sep. 2006, pp. 212–215.

[35] J. R. Lane, R. G. Freitag, Hyo-Kun Hahn, J. E. Degenford, and M. Cohn, "High- efficiency 1-, 2-, and 4-W class-B FET power amplifiers," *IEEE Trans. Microw. Theory Techn.*, vol. MTT-34, no. 12, pp. 1318–1326, Dec. 1986.

[36] Y. Sun and A. P. Freundorfer, "Broadband folded Wilkinson power combiner/splitter," *IEEE Microw. Wireless Compon. Lett.*, vol. 14, no. 6, pp. 295–297, Jun. 2004.

[37] B. Razavi, *RF Microelectronics*, 2nd ed., Upper Saddle River, NJ, USA: Prentice-Hall, 2012.

[38] H. Ku and J. S. Kenney, "Behavioral modeling of nonlinear RF power amplifiers considering memory effects," *IEEE Trans. Microw. Theory Techn.*, vol. 51, no. 12, pp. 2495–2504, Dec. 2003.

[39] J. H. K. Vuolevi, T. Rahkonen, and J. P. A. Manninen, "Measurement technique for characterizing memory effects in RF power amplifiers," *IEEE Trans. Microw. Theory Techn.*, vol. 49, no. 8, pp. 1383–1389, Aug. 2001.

[40] C. A. Balanis, *Antenna Theory: Analysis and Design*, 4th ed., Hoboken, NJ, USA: Wiley, 2016.

[41] W. L. Stutzman and G. A. Thiele, *Antenna Theory and Design*, 3rd ed., Hoboken, NJ, USA: Wiley, 2013.

[42] H. L. Van Trees, *Optimum Array Processing: Part IV of Detection, Estimation, and Modulation Theory*. Hoboken, NJ, USA: Wiley, 2002.

[43] E. Björnson and Ö. T. Demir, *Introduction to Multiple Antenna Communications and Reconfigurable Surfaces*. Boston, MA, USA: Now, 2024.

[44] C. K. Alexander and M. N. O. Sadiku, *Fundamentals of Electric Circuits*, 5th ed., New York, NY, USA: McGraw-Hill, 2013.

MARIUS DIACU (Graduate Student Member, IEEE) received the B.Sc. and M.Sc. degrees in electrical and computer engineering from the NOVA School of Science and Technology (NOVA SST), NOVA University of Lisbon, in 2023 and 2025, respectively, where he is currently pursuing the Ph.D. degree. His current research interests include energy-efficient transmitter designs, spatial signal processing, compensation of nonlinear distortion effects, and receiver design. He has published two conference papers. He has received two grants, for exceptional academic performance with the NOVA University of Lisbon.

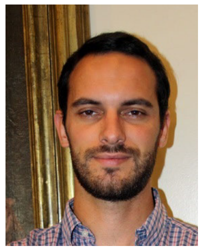

JOÃO GUERREIRO (Member, IEEE) received the M.Sc. and Ph.D. degrees in electrical and computer engineering from the Faculdade de Ciências e Tecnologia (FCT), Universidade Nova de Lisboa (UNL), in 2012 and 2016, respectively. He is currently an Assistant Professor with FCT-UNL and a Researcher with the Instituto de Telecomunicações. Since 2013, he has been actively involved in scientific research in wireless communications, including signal processing, transceiver design, and channel modeling. He published over 30 journal articles, 60 conference papers (one best paper award), three patents (granted or pending), and two book chapters. He has participated in several national and international research projects in the last few years. He is an Editor of IEEE Communications Letters.

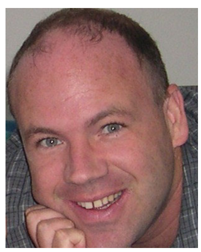

RUI DINIS (Senior Member, IEEE) received the Ph.D. degree from the Instituto Superior Técnico (IST), Technical University of Lisbon, Portugal, in 2001, and the Habilitation degree in telecommunications from the Faculdade de Ciências e Tecnologia (FCT), Universidade Nova de Lisboa (UNL), in 2010. From 2001 to 2008, he was an Assistant Professor with IST. In 2003, he was an Invited Researcher with Carleton University, Ottawa, Canada. He was a Researcher with the Centro de Análise e Processamento de Sinal (CAPS), IST, from 1992 to 2005; and a Researcher with the Instituto de Sistemas e Robótica (ISR), from 2005 to 2008. He is currently a Full Professor with FCT-UNL. Since 2009, he has been a Senior Researcher with the Instituto de Telecomunicações (IT). His research interests include transmission, estimation, and detection techniques for wireless communications. He is or was an editor of IEEE Transactions on Wireless Communications, IEEE Transactions on Communications, IEEE Transactions on Vehicular Technology, IEEE Open Journal of the Communications Society, and *Physical Communication* (Elsevier). He was also a guest editor for several special issues. He is a VTS Distinguished Speaker and a ComSoc Distinguished Lecturer.

JOÃO P. OLIVEIRA (Member, IEEE) received the M.Sc. and Ph.D. degrees in microelectronics and telecommunications. In 2003, he joined the Department of Electrical Engineering, NOVA FCT, NOVA University of Lisbon, where he is currently an Associate Professor of electronics and microelectronics. He is also a Senior Researcher with the Centre of Technology and Systems (CTS), UNINOVA, focusing on the design of mixed-signal integrated circuits in nanoscale CMOS technology for radio and the IoT applications. He has over five years of industry experience in the telecommunications sector, where he was actively involved in the development and deployment of early 3G radio networks. Beyond academia, he co-founded Mobbit Systems, where he led the development of hardware and software for smart sensorial interactive the IoT systems. He is also a Co-Founder of Koala Tech, a NOVA Spin-Off startup specializing in highly efficient RF power amplifiers based on quantized digital amplification (QDA), a technology patented by the founding team. He has published in international journals and conferences, authored two books, and holds four patents. His research interests include low-power, low-voltage RF-CMOS mixed-signal integrated circuits and analog front-ends for the IoT sensing ecosystems, leveraging disruptive techniques, such as MOS parametric-based signal processing. He is affiliated with the Solid-State Circuits Society (SSCS), the Circuits and Systems Society (CAS), the Communications Society (ComSoc), and the Microwave Theory and Technology Society (MTT-S).

PAULO MONTEZUMA received the Ph.D. degree from the Faculdade de Ciências e Tecnologia (FCT), Universidade Nova de Lisboa (UNL), Portugal. From 2001 to 2013, he was a Researcher with UNINOVA. In 2013, he joined Instituto de Telecomunicações. He is currently an Associate Professor with FCT-UNL and a Researcher with the Instituto de Telecomunicações, Lisbon. He has been actively involved in several international research projects in the wireless communications area. His main research activities are on transmitter design, coding and receiver design, namely for MIMO systems, OFDM, and SC-FDE modulations.

PEDRO VIEGAS received the M.Sc. degree in electrical and computer engineering from the Faculdade de Ciências e Tecnologia (FCT), Universidade Nova de Lisboa (UNL), in 2017. He is currently a postgraduate in applied business management from the Nova School of Business and Economics (Nova SBE). From January 2018 to April 2019, he was an IT Researcher with the Instituto de Telecomunicações, working on projects, such as multilayer massive MIMO systems for the fifth generation (5G) wireless communications (MM5G) and Power Efficient Solutions for secure wireless sensor networks (PES3N). He has a Project Management training certificate from Nova SBE. Since May 2019, he has been a Signal Processing Engineer with Koala Tech, working on multi-branch amplification structures and quantized amplification schemes, multi-carrier/single-carrier signals, and M-QAM signal modulation. At Koala Tech, he is also a Founding Member, Marketing Coordinator, and Internationalization Coordinator.